Modelling the complete life cycle of an arctic copepod reveals complex trade-offs between concurrent life cycle strategies

Catherine E. Brennan, Frédéric Maps, Diane Lavoie, Stéphane Plourde, Catherine L. Johnson

Progress in Oceanography 229 (2024) 103333

Contents lists available at ScienceDirect

Progress in Oceanography

journal homepage: www.elsevier.com/locate/pocean

Modelling the complete life cycle of an arctic copepod reveals complex trade-offs between concurrent life cycle strategies

Catherine E. Brennan [a,*], Frédéric Maps [b], Diane Lavoie [c], Stéphane Plourde [c], Catherine L. Johnson [a]

[a] Fisheries and Oceans Canada, Bedford Institute of Oceanography, PO Box 1006, Dartmouth, NS B2Y 4A2, Canada
[b] Takuvik Joint International Laboratory, Université Laval (Canada) – CNRS (France)/Québec-Océan/Département de Biologie at Université Laval, 1045 Avenue de la Médecine, Québec, QC G1V 0A6, Canada
[c] Fisheries and Oceans Canada, Maurice Lamontagne Institute, 850 Route de la Mer, Mont-Joli, QC G5H 3Z4, Canada

ARTICLE INFO

Keywords:
Population dynamics
Mathematical models
Individual based model
Zooplankton
Calanus hyperboreus
Life history
Northwest Atlantic
Gulf of St. Lawrence

ABSTRACT

Calanus hyperboreus is a large-bodied, biomass dominant species that performs a crucial ecosystem energy transfer by converting the spring phytoplankton bloom into lipid reserves that fuel the higher trophic levels of the Gulf of St. Lawrence (GSL) pelagic ecosystem, including the critically endangered North Atlantic right whale (*Eubalena glacialis*). Given that the GSL, the southernmost core habitat of *C. hyperboreus*, is undergoing rapid warming, developing a population model allows us to synthesize existing knowledge of the species, and to examine the species response to environmental conditions. To simulate the multi-year life cycle in the northwest GSL, model equations are implemented for ingestion, assimilation, respiration, egg production, stage development, mortality, and vertical migration behaviors including dormancy entry and exit. The 1-D particle-based model predicts the evolution of individual stage, structural mass, lipid, age, sex, abundance, and egg production, as well as the seasonal evolution of the population structure in the northwest GSL. Individual lipid-based thresholds inform the timing of ontogenetic vertical migration. Life cycle targets defined from a literature review are used to guide model parameterization and assess its performance. The simulated population structure, phenology, and size at stage are generally consistent with observations. Under 10 years of repeat year forcing, the model simulates a quasi-stable overwintering population composed of late stages CIV, CV and CVI. Observations suggest that stage CIV is the first overwintering stage in the GSL, and point to the occurrence of iteroparous females. Using the model, the relative success of diverse dormancy and reproductive phenotypes are explored. Second reproduction females reproduce earlier in winter than first reproduction females, with implications for the ability of the new generation to match the spring bloom and accumulate sufficient lipid to overwinter as stage CIV. Without iteroparity, the time window of reproduction contracts and the population is reduced, underscoring the role of a flexible multi-year life cycle in population success.

1. Introduction

Calanus hyperboreus is a cornerstone zooplankton species (*Copepoda*) in the Gulf of St. Lawrence (GSL) ecosystem, where it dominates the biomass of mesozooplankton (Blais et al. 2021). It performs a crucial energy transfer by converting the brief and intense phytoplankton spring bloom into structural growth and lipid stores, supporting higher trophic levels (Falk-Petersen et al. 1990), including planktivorous fish and North Atlantic right whales (*Eubalaena glacialis*). Lipid stores support the metabolic requirements of *C. hyperboreus* during a >6 month dormancy at depth and its adult reproduction as a capital breeder at the end of dormancy (Conover 1988, Hirche & Niehoff 1996, Scott et al. 2000). At the southernmost end of the reproductive range of *C. hyperboreus* in the western Atlantic (Conover 1988, Sameoto & Herman 1990, Plourde et al. 2003), this population may be particularly vulnerable to warming and other changes in the marine environment caused by anthropogenic climate change (Galbraith et al. 2022). Substantial warming of the GSL deep water observed post-2010 at the species overwintering depth

* Corresponding author.
E-mail addresses: Catherine.Brennan@dfo-mpo.gc.ca (C.E. Brennan), frederic.maps@bio.ulaval.ca (F. Maps), Diane.Lavoie@dfo-mpo.gc.ca (D. Lavoie), Stephane.Plourde@dfo-mpo.gc.ca (S. Plourde), Catherine.Johnson@dfo-mpo.gc.ca (C.L. Johnson).

https://doi.org/10.1016/j.pocean.2024.103333
Received 21 February 2024; Received in revised form 13 June 2024; Accepted 15 August 2024
Available online 27 August 2024

(Brickman et al. 2018, Galbraith et al. 2022) is projected to continue over the 21st century with a trend of ~+0.7 ℃ per decade at 150–300 m (Lavoie et al. 2020). Warmer water increases *C. hyperboreus* female metabolic demand which more rapidly depletes the lipid reserve, resulting in less lipid available for reproduction, and earlier, shorter spawning (Plourde et al. 2003, Schultz et al. 2020). As an Arctic species, the *C. hyperboreus* life cycle is tightly linked to the extreme seasonality of its local environment. The timing of the spring bloom is hypothesized to influence its multi-year life cycle, which can vary from 1 to 5 years, and its first overwintering stage as CIII, CIV, or CV (Falk-Petersen et al. 2009). It remains highly uncertain as to how this large-bodied species with high phenological and physiological plasticity (Kvile et al. 2018) may respond to the impacts of climate change. Marine animals typically encounter ocean warming near the sea surface, but warming deep water in the GSL is likely to significantly affect *C. hyperboreus* due to its long overwintering periods at depth. Anthropogenic changes documented in the GSL include deep water warming, near surface warming, reduced sea ice, and enhanced stratification (Galbraith et al. 2022), while biogeochemical models project declines in phytoplankton production and an earlier spring bloom in most sub-regions of the GSL by the end of the 21st century (Lavoie et al. 2020, Mei et al. 2024). Validating our understanding of the *C. hyperboreus* life cycle in the GSL (Plourde et al. 2003, Blais et al. 2021), and how this population responds to environmental change is urgent.

One implication of the ontogenetic vertical migration behavior of late-stage copepodites of *Calanus* spp., characterized by multiple months spent overwintering at depth, is that the population exhibits complex responses to environmental change. *C. hyperboreus* has the potential to outlast starvation and eventually reproduce despite poor conditions in any given year, thanks to its large lipid stores that support its multi-year life cycle – a so-called 'buffering' capability. What kind of environmental changes could lead to a disruption of the species buffering capability remains an open question. Testing hypotheses about the species complex and long-term response to environmental forcing using ship-based sampling remains extremely challenging. Generally, a numerical model representing the *C. hyperboreus* life cycle allows an exploration of the species' potential vulnerabilities and range of responses to environmental change over different temporal and spatial scales.

Ship and lab-based studies underpin the present understanding of *C. hyperboreus* distribution and biology (Conover 1962, 1965a, 1967, 1988, Conover & Corner 1968, Dawson 1978, Head & Harris 1985, Head et al. 1986, Hirche 1991, Conover & Huntley 1991, Hirche & Niehoff 1996, Kosobokova et al. 1997, Melle & Skjoldal 1998, Scott et al. 2000, Ikeda et al. 2001, Pasternak et al. 2001, Ringuette et al. 2002, Takahashi et al. 2002, Ashjian et al. 2003, Plourde et al. 2003, Lee et al. 2006, Davies et al. 2012), while modelling has helped to quantify and understand different aspects of the *C. hyperboreus* biology and life cycle since the pioneering work of Carlotti and Slagstad (1997). Simulating the full life cycle of this long-lived species requires both realistic functional forms and parameter values that accurately inform the model on the individual's metabolism (Plourde et al. 2003) and development duration, both during the active development phase (Ji et al. 2012) and the prolonged dormancy (Maps et al. 2014a). Moreover, such a model needs to keep track of the individual body mass, and it is also useful to differentiate between the body structural mass (*i.e.*, lean mass) and lipid stores (Maps et al. 2012b, Bandara et al. 2018, Aarflot et al. 2022). While *C. hyperboreus* models have increased in scope and complexity over time, all previous models have neglected at least one key property (*i.e.*, lipid content as a fully free-evolving variable) and/or imposed *a priori* key behavior (*i.e.*, timing of diapause entry and exit).

The goals of this study are to (i) review the *C. hyperboreus* life cycle in the GSL in the context of its regional ecology and environmental pressures; (ii) build and apply a one-dimensional (1-D) *C. hyperboreus* population model in the northwest GSL to test our knowledge of its life cycle; and (iii) identify key population characteristics through the model-building process and subsequent simulation analysis for this species that is less studied compared to its congener, *C. finmarchicus*. We expect to learn from the sensitivity analysis and model simulations how the environment structures the *C. hyperboreus* life cycle in the GSL, including the first overwintering stage as CIV and the reproductive pulse from second reproduction females – $CVIF_{R2}$, defined as females that return to the surface to feed and rebuild lipid stores following reproduction at depth, and then subsequently enter dormancy as adults. In the model, food assimilation, lipid accumulation, and respiration are likely to be important processes for this large, lipid-rich species. We thus expect the model to be especially sensitive to the representation of lipids, including which stages can grow reserves and their maximum lipid content, the lipid thresholds chosen for dormancy entry and exit, and the lipid accumulation rate.

2. Approach

A combination of literature review and data synthesis informed the development of a *C. hyperboreus* life cycle model for the GSL. We first reviewed the *C. hyperboreus* literature describing the species physical properties, behavior, and phenology, noting how its life history varies (*i.e.*, its plasticity), across its biogeographic range from the high Arctic (Lee 1974, Dawson 1978, Smith 1988, Melle & Skjoldal 1998, Falk-Petersen et al. 2009, Schmid et al. 2018) to the GSL, and even into the Gulf of Maine during a cold period in the 1960s (Conover 1962). We then drew upon regional datasets to situate the GSL population in the context of its Arctic and Atlantic range. We used this information to develop a conceptual model of the *C. hyperboreus* life cycle in the GSL (Fig. 1) in terms of the timing of key life history events as well as metrics of its dormancy strategy, size and population structure. The equations we derived from this exercise consolidate what is empirically known, with assumptions about what is unknown. By sharing the knowledge gained through the process of model building and analysis, we can identify key biological variables to other modellers, generate new testable hypotheses, and inform future zooplankton sampling priorities. Simulating the full life cycle of *C. hyperboreus* in the GSL is a first step toward predicting how the population and its role in the marine ecosystem may shift in response to climate change in a rapidly warming GSL.

To develop the numerical model of the *C. hyperboreus* population in the GSL, we started from the core model equations and parameterizations described in Bandara et al. (2019). However, to capture the observed population dynamics in the GSL we adapted that previous model when necessary, primarily in implementing a different maximum lipid content and changes to the biological equations or parameters affecting respiration, ingestion, mortality, and other processes described below. Specific biological and phenological components of our conceptual model for the *C. hyperboreus* life cycle in the GSL were selected as "targets" for the calibration of the *C. hyperboreus* population model. Sensitivity experiments and comparison of model output with data allowed an iterative process of model improvement highlighting which model processes were most important for simulating the species dynamics, that ultimately produced a quasi-stable *C. hyperboreus* population consistent with observed patterns in the GSL. The *C. hyperboreus* population structure was simulated in a set of experiments under repeat-year forcing, with and without second reproduction females, to investigate how the entire population and different dormancy phenotypes, including overwintering CIVs and iteroparous females, respond to the local environment.

2.1. Site description and hydrography: Anticosti Gyre Station, northwest GSL

The model is implemented in the northwest GSL in a 1-D configuration at the Anticosti Gyre Station (49.72N, 66.25W, ~350 m water depth), as indicated in Fig. 1 (inset map). Despite its location at the southern margin of the species biogeographical range, the GSL is a unique environment which represents the whole range of environmental

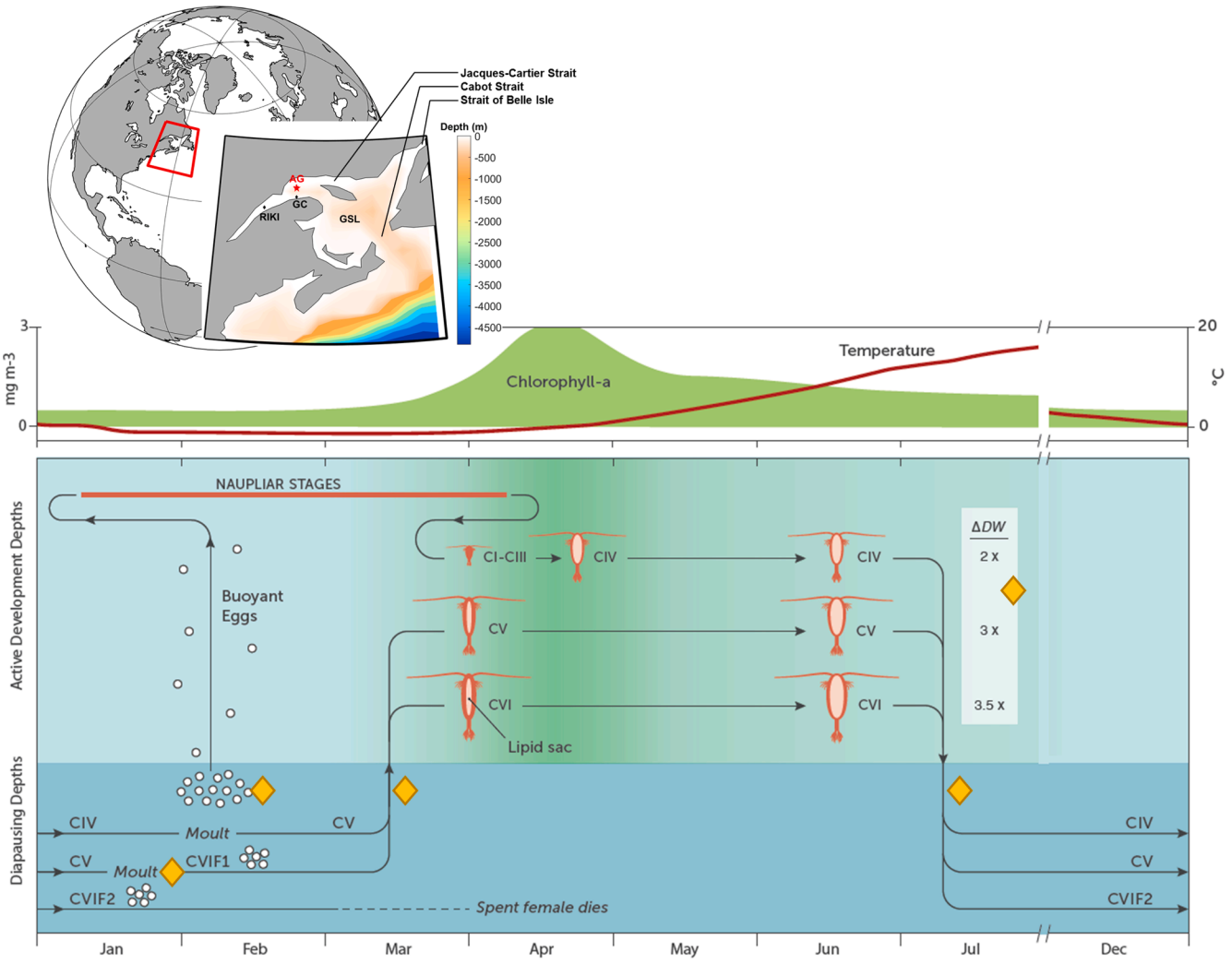

Fig. 1. Schematic of our conceptual model for key life cycle processes of the *C. hyperboreus* population in the Gulf of St. Lawrence (GSL; inset map indicates station locations in the northwest GSL and LSLE: AG=Anticosti Gyre (red star), GC=Gaspé Current, RIKI=Rimouski). A typical seasonal cycle of food (green shading) and temperature (red line) for the northwest GSL is indicated in the top panel. Reproduction and growth of early stages occur pre-spring bloom when temperatures are relatively cold. Eggs are produced at depth, rise buoyantly to the near surface, and develop through six naupliar stages (NI-NVI) and the early copepodite stages (CI-CIII). Development beyond the first feeding stage, NIII, depends on food availability, with growth and/or lipid accumulation during the bloom resulting in dry weight increases (ΔDW) for late-stage copepodites. The new generation migrates to depth and enters dormancy primarily as stage CIV in early July (post-bloom) when temperature is high. For dormant CIV and CV, molt to the next stage occurs at depth at the end of the overwintering period, and the terminal molt to adult (CVI) is followed by gonad development in 'first reproduction females' ($CVIF_{R1}$). After reproduction at depth, females are spent and die, or else they can ascend to the surface and resume feeding, following an iteroparous strategy as 'second reproduction females' ($CVIF_{R2}$). $CVIF_{R2}$ undergo a second egg production at the end of dormancy, after which females are spent and die. Life cycle events defined as "targets" for the population model are indicated by yellow diamonds: timing of molt to adult, egg production, and diapause exit and entry, and size differences post- vs pre-bloom. Inset maps were created using M_Map (Pawlowicz, 2020). Schematic graphic design was provided by John Newgard.

conditions the species can encounter, from warm Atlantic to cold Arctic waters, except for the long darkness of the high Arctic region. The GSL is influenced by the freshwater outflow from the St. Lawrence River, as well as Atlantic water contributions arriving through the Strait of Belle Isle and Cabot Strait, and it is historically covered with sea ice for multiple months in winter (Koutitonsky & Bugden 1991). The northwest GSL is part of a larger zooplankton 'circuit' involving the Lower St. Lawrence Estuary (LSLE) to the west and inputs from Arctic-sourced water masses via Jacques-Cartier Strait to the east, forming a quasi-Arctic biome that is structured in part by the estuarine sheared circulation (Maps et al. 2014b, Lavoie et al. 2016, Benkort et al. 2020, Le Corre et al., 2023). The water mass structure is strongly seasonal, and influenced by the presence of sea ice from ~ January to March. The winter water column consists of two distinct layers, with a cold upper layer (from −1.8 ℃ below the sea ice to 0–1 ℃) extending over the top 50–75 m, and a warmer Atlantic water layer (4–6 ℃) below (Trites & Walton 1975). The near surface warms following sea ice melt in early spring, while a remnant cold intermediate layer is preserved beneath it, overlying the warmer Atlantic water layer at depth, forming a three-layer system in summer (Galbraith et al. 2022). Implementing the model in 1-D at the Anticosti Gyre station allows us to simulate a deep site in the center of the northwest GSL that is relatively well sampled and hosts a persistent population, as indicated by high abundance of *C. hyperboreus* throughout the year (Plourde et al. 2014). In the GSL, riverine outflow moves seaward in the surface layer, balanced by a return flow at depth of warm, saline Atlantic water (Koutitonsky & Bugden 1991). This estuarine circulation is apparent in the contrast between the ~ 4.8 year transit time of deep water from Cabot Strait to the LSLE (Budgen 1991) and the ~ 100 day time scale for St. Lawrence River discharge to exit the GSL via Cabot Strait in the surface layer (Trites &

Walton 1975, Ohashi & Sheng 2013). 1-D models of biogeochemical and copepod dynamics were previously implemented at the Anticosti Gyre station (Tian et al. 2000, Maps et al. 2012a), as the location is not directly impacted by the St. Lawrence River outflow concentrated in the Gaspé Current to the south (Koutitonsky & Bugden 1991, Tian et al. 2000), though salinity in the northwest GSL responds to variations in freshwater discharge (Ohashi & Sheng 2013). The seasonal cycles of surface temperature in the GSL (Galbraith et al. 2022) and chlorophyll-a in the northwest GSL (Blais et al. 2021) are shown in Fig. 1.

3. Review of the *C. hyperboreus* life cycle

In this section, we review the life cycle of *C. hyperboreus* and identify life cycle targets for model development and validation. The targets include literature- and data-derived estimates of the species characteristics and properties (size, rates, phenology) in the GSL. Here we provide a comprehensive description of the species and its ecological range. In comparison to its smaller congener *C. finmarchicus*, fewer studies focused on *C. hyperboreus*, whose multi-year life cycle essentially precludes the possibility of raising individuals from egg to mature adult in the lab. Nevertheless, previous investigators have provided substantial understanding of the *C. hyperboreus* biology, behavior, and ecology.

3.1. Species distribution and Adaptation

C. hyperboreus is distributed throughout the North Atlantic and the Arctic, typically associated with deep basins and cold water. High abundances have been found in the Arctic and sub-Arctic North Atlantic, including the Barents Sea, Greenland-Iceland-Norwegian seas, Labrador Sea, Baffin Bay, Gulf of St. Lawrence, Scotian Shelf and Gulf of Maine (see *meta*-analysis distribution map of Visser et al. (2017)). The species is adapted to survive long Arctic winters under ice cover, characterized by periods of darkness with low food availability, and once the sea ice melts, to convert the brief and variable phytoplankton spring bloom into growth and lipid stores (Scott et al. 2000, Falk-Petersen et al. 2009). This capital breeder utilizes stored lipid to spawn ahead of the spring bloom, in late autumn and winter (Smith 1990, Schultz et al. 2020). Eggs develop through six naupliar stages (NI-NVI) and six copepodite stages (CI-CVI), with the adult stage being CVI. During the spring bloom, high food concentrations enable rapid growth, as well as lipid accumulation for the stages $\geq$ CIII bearing lipid sacs (Pasternak et al. 2001, Plourde et al. 2003). Once the new generation develops to the first overwintering stage and the bloom has ended, lipid-rich late stages leave the surface waters to overwinter at depth (Hirche 1998).

3.2. Multiyear life cycle and dormancy

A key characteristic of *C. hyperboreus* is its multiyear life cycle, which spans from 1-2 years to up to 4–6 years (Falk-Petersen et al. 2009, Hirche 2013). *C. hyperboreus* performs a seasonal vertical migration and can remain at depth with a reduced metabolism for multiple months while surface conditions are unfavorable, supported by the lipid reserve contained in its lipid sac (Conover 1962, Auel et al. 2003). *Calanus* spp. perform 'classical' diapause with no feeding or swimming and arrested development in mesopelagic environments (>600 m depth), (Hirche 1996, Falk-Petersen et al. 2009, Baumgartner & Tarrant 2017). In contrast, in shallow shelf seas (<200 m) *Calanus* enter a "winter resting state" with measurable locomotor activity (Coguiec et al. 2023). In the GSL, *C. hyperboreus* dormancy can occur on shallow shelves or in deep channels (250–500 m) (Krumhansl et al. 2018, Plourde et al. 2019). The first dormancy stage is shaped by the local environment, as the new generation must develop from the first feeding stage to the first dormancy stage within the active growth period, and accumulate sufficient lipid to support the overwintering metabolic requirements (Ejsmond et al. 2018). Alternatively, lipid-poor individuals may enter dormancy but ascend early into a surface active layer with unfavorable conditions, incurring higher mortality risk relative to the safety associated with overwintering (*i.e.*, overwintering mortality is 10% that experienced by active individuals; McLaren et al. 2001, Maps et al. 2010, Varpe & Ejsmond 2018b). *C. hyperboreus* first enters dormancy at stage CIII in the eastern Canadian Arctic, Greenland Sea and central Arctic (Dawson 1978, Longhurst et al. 1984, Hirche 1997, Ashjian et al. 2003), at stage CIV in the GSL (Plourde et al. 2003), or at stage CV as in the Gulf of Maine (Conover 1988). Molting to the subsequent copepodite stage occurs at depth at the end of the overwintering period, based on data from the GSL (described below), followed by ascent to the near surface.

The *C. hyperboreus* life cycle can be described by the species' dormancy strategy, along with key metrics related to size and timing (Fig. 1, Table 1). Dormancy strategy includes both the first overwintering stage, and whether or not females return to the near surface following reproduction, generating second reproduction females (*i.e.*, iteroparity). In the GSL, the first overwintering stage is CIV, and an individual may sequentially overwinter as stage CV and CVI (3-year life cycle) such that the population in diapause consists of stages CIV-CVI (Plourde et al. 2003). Plourde et al. (2003) showed the overwintering population stage composition during the 1990′s was dominated by high proportions of CIV, CV, and CVI, with trace abundances of CIII. Evidence for iteroparity in the GSL was based on their female dry weight distribution, which suggested active season growth of females. An alternate life history path may be followed by lipid poor stage CIV individuals that develop to CV before entering dormancy (2-year life cycle). In the absence of a second reproduction female strategy, the life cycle described above is one year shorter and females newly molted from overwintering CVs are energetically spent after completing egg production and die at depth (1–2-year life cycle).

Since dormancy timing responds to both the variable food supply and the mortality risk experienced by active individuals (Varpe & Ejsmond 2018b), spatial variation is expected based on the regional timing of the spring bloom, the bloom duration, post-bloom food availability, and the local predator field, while dormancy duration is also influenced by temperature and ultimately constrained by the size of the individuals' lipid reserve (Saumweber & Durbin 2006, Pierson et al. 2013). The lipid accumulation window (LAW) hypothesis posited that late-stage *Calanus* must acquire a sufficient lipid amount to enter dormancy (Rey-Rassat et al. 2002, Maps et al. 2010, 2012a) and fuel basal metabolism during the multiple months spent overwintering (Hirche 1996), as well as gonad development for newly molted females (Jónasdóttir 1999). In the case of the capital breeder *C. hyperboreus*, lipid stores are also catabolized to support egg production (Hirche & Niehoff 1996). Other potential factors have been proposed to potentially influence dormancy entry timing, including environmental conditions (*i.e.*, photoperiod, food concentration, temperature) and cues internal to the organism such as hormonal levels or gene expression, which in turn are potentially influenced by the individual lipid level (Häfker et al. 2018) or other external factors such as predation (Skottene et al. 2020). While only lipid levels could not be ruled out as a driver in an empirical analysis of *C. finmarchicus* dormancy timing across the northwest Atlantic (Johnson et al. 2008), it remains unknown as to whether these additional factors may play a role. This uncertainty is especially high for *C. hyperboreus* whose dormancy is less well characterized (Baumgartner & Tarrant 2017), and whose phenology in the GSL appears to be more synchronous than *C. finmarchicus*.

Phenology metrics used for model targets describe when key events or transitions occur, including the timing of CV molt to adult, female egg production, CIV molt to CV and exit from dormancy, and entry into dormancy for late stages (CIV-CVI) (Table 1). Dormancy timing was estimated for *C. hyperboreus* CIV-CVI in the northwest GSL using observations from the Atlantic Zone Monitoring Program (AZMP) (Therriault et al. 1998), based on zooplankton net sampling at high-frequency fixed stations and biannual transect stations. Climatological staged abundance (ind. m^2) and staged proportions (range = 0–1) were predicted by a loess model fit using the R function 'smooth' to the

Table 1
Targets selected from the *C. hyperboreus* life cycle schematic for the model to simulate. Metrics are grouped by dormancy strategy, mean size of late stages during the pre-bloom and post-bloom periods, and phenology. For each target, the values or ranges derived from literature and data are listed (center column), and the sources used to inform the literature/data targets are indicated in the footnote. The corresponding model output from the final year of the baseline simulation is included for comparison (right column). We refer to size metrics with DW=dry weight, C=carbon. Note that DW is reported in the literature units of µg, while the model output is converted into µg from units of µg C assuming late stage individual DW is 60% C after Smith (1990). The model values in units of µg C are provided in parentheses. We report only $CVIF_{R2}$ from the model, because the observed females were actively growing in the post-bloom period[1].

	Metric	Literature/Data Target	Model (final year)
Dormancy strategy	**First dormant stage**	CIV [1]	CIV and CV
	Second year females (iteroparity)	Occurs [1]	Occurs in baseline simulation
Size	**CIV DW (µg)**	Pre-bloom 300 [1,2] Post-bloom 650 [1,2]	Pre-bloom 504 (303 µg C) Post-bloom 924 (554 µg C)
	CV DW (µg)	Pre-bloom 700 [1] Post-bloom 2100 [1]	Pre-bloom 1470 (882 µg C) Post-bloom 2177 (1306 µg C)
	CVIF DW (µg)	Pre-bloom 1000 [1] Post-bloom 3500 [1]	$CVIF_{R2}$ Pre-bloom 1810 (1086 µg C) $CVIF_{R2}$ Post-bloom 2755 (1653 µg C)
Phenology	**CI-CIII peak abundance**	Coincides with spring bloom [1], which on average starts on April 11th and lasts 37 days in the northwest GSL [3]	April-May, coincides with spring bloom in model forcing starting April 9th
	Peak diapause entry	June-early July [4]	CIV June, CV June-September, $CVIF_{R2}$ May-June
	Terminal molt (CV to adult) and egg production (EP)	January-March [1,4]	Molt to adult: late January-mid-April, EP peak: January-March, EP range: late November-April
	CIV to CV molt and dormancy exit	March [4]	January - April

Sources of literature- and data-based targets: 1. Plourde et al. 2003; 2. Le Corre et al., 2023; 3. Blais et al. 2021; 4. AZMP data shown in Fig. 2: peak diapause entry is based on the activity index (Fig. 2p-r); terminal molt timing is based on the maximum abundance of males (Fig. 2a); egg production timing is based on GSL egg production experiments in Plourde et al. 2003; timing of CIV molt to CV and exit from diapause is based on the changes in CIV and CV abundance and the CIV minimum abundance (Fig. 2c-d).

observations collected during the years 1999–2021 at the Rimouski (RIKI) and Gaspé Current (GC) stations (Fig. 2 panels I-II). Vertically stratified sampling at RIKI during the years 2004–2010 and 2021 (Fig. 2 panel III) informed a late-stage activity index, by fitting a loess model to the climatological staged abundance proportion in the upper 125 m of the 320 m water column. Note that data analysis was performed by Stéphane Plourde and Caroline Lehoux, and no vertically stratified data were collected during the first 60 days due to sea ice. Based on visual inspection of the activity index, the dormancy timing was estimated for *C. hyperboreus* in the northwest GSL (Fig. 2 panel IV). To highlight the peak timing of descent, a red box was placed by hand such that its edges extend from the date when the smoothed mean diverges from the active period variability, to the start of diapause period variability, and the box center is indicated (gray vertical line). The AZMP abundance climatology served to identify the March timing of CIV to CV molt and dormancy exit, based on the respective decrease and increase in CIV and CV abundance (Fig. 2 panel I), which corresponds to ~ 8 months overwintering. The high relative abundance of males (CVIM) in January-February indicated the peak molt from CV to adult (Fig. 2 panels I-III). Molting was determined to occur at depth based on the timing of the terminal molt and CIV-CV molt, when CIV-CVI and all CIV respectively are observed only at depth (Fig. 2n,p, see also Plourde et al. (2003)). Spawning occurs at depth mainly in January-March, as determined from the incubation experiments using females collected from the LSLE in mid-December (Plourde et al. 2003). By comparison, in the Greenland Sea, the diapause duration extends ~six months from September-March (Hirche 1997, Baumgartner & Tarrant 2017). The schematic of the *C. hyperboreus* life cycle in the GSL (Fig. 1) includes yellow diamonds to indicate the phenology targets described above.

3.3. Energy dynamics: ingestion, assimilation, lipid accumulation, respiration

As the largest congener of the *Calanus* spp., *C. hyperboreus* females are capable of growing up to 6 mg dry weight (DW), although typical sizes range from ~1 mg when females are spent following egg production, to 2–5 mg at the start of diapause (Lee 1974, Conover & Huntley 1991, Scott et al. 2000, Auel et al. 2003, Plourde et al. 2003). Growth results from the balance of inputs (assimilation, equivalent to ingestion minus egestion) and outputs (respiration/excretion, egg production), and depends on the environment through food availability and biological rate dependencies on temperature. The observed seasonal evolution of body size in the GSL indicates that the late stages are at their minimum dry weight at the end of the overwintering period and just prior to the spring bloom. This is followed by rapid growth of late stages during the spring bloom when mean dry weights increase relative to the pre-bloom period by a factor of 2, 3, and 3.5 for CIV, CV, and females, respectively (Plourde et al. 2003). Typically considered an herbivore, *C. hyperboreus* mainly consumes phytoplankton, but ingestion of microzooplankton also occurs (Campbell et al. 2009). Eggs spawned in advance of the spring bloom develop to NIII, the first feeding stage, and while food is required for development to the next stage, stage NIII survived without food for ~1 month in lab experiments (Jung-Madsen et al. 2013). A typical food assimilation rate for copepods is two-thirds (Kiørboe 2008), and for *C. hyperboreus* Conover 1966 reported ~70%, with diverse food types yielding variable mean values of 40.1–86.7% (1966). Respiration generally scales with total mass raised to ¾ power (Kiørboe 2008), although it is questionable whether metabolically inactive lipid stores should be included. Respiration rates increase with temperature and vary seasonally, with overwintering values ~25% that of active values (Maps et al. 2014a). When inputs exceed outputs, net growth is apportioned to the body structure, which is lean mass, or in the case of late stages bearing lipid sacs, growth can be stored as wax ester-dominated lipid (Lee 1974). Lipid accumulated in excess of the diapause metabolic requirements can be utilized to support adult gonad development and maturation and egg production (Conover 1965b, Hirche & Niehoff 1996, Schultz et al. 2020). Female lipid content varied from 15% to >70% of DW in the Gulf of Maine (Conover 1962), while in the Arctic

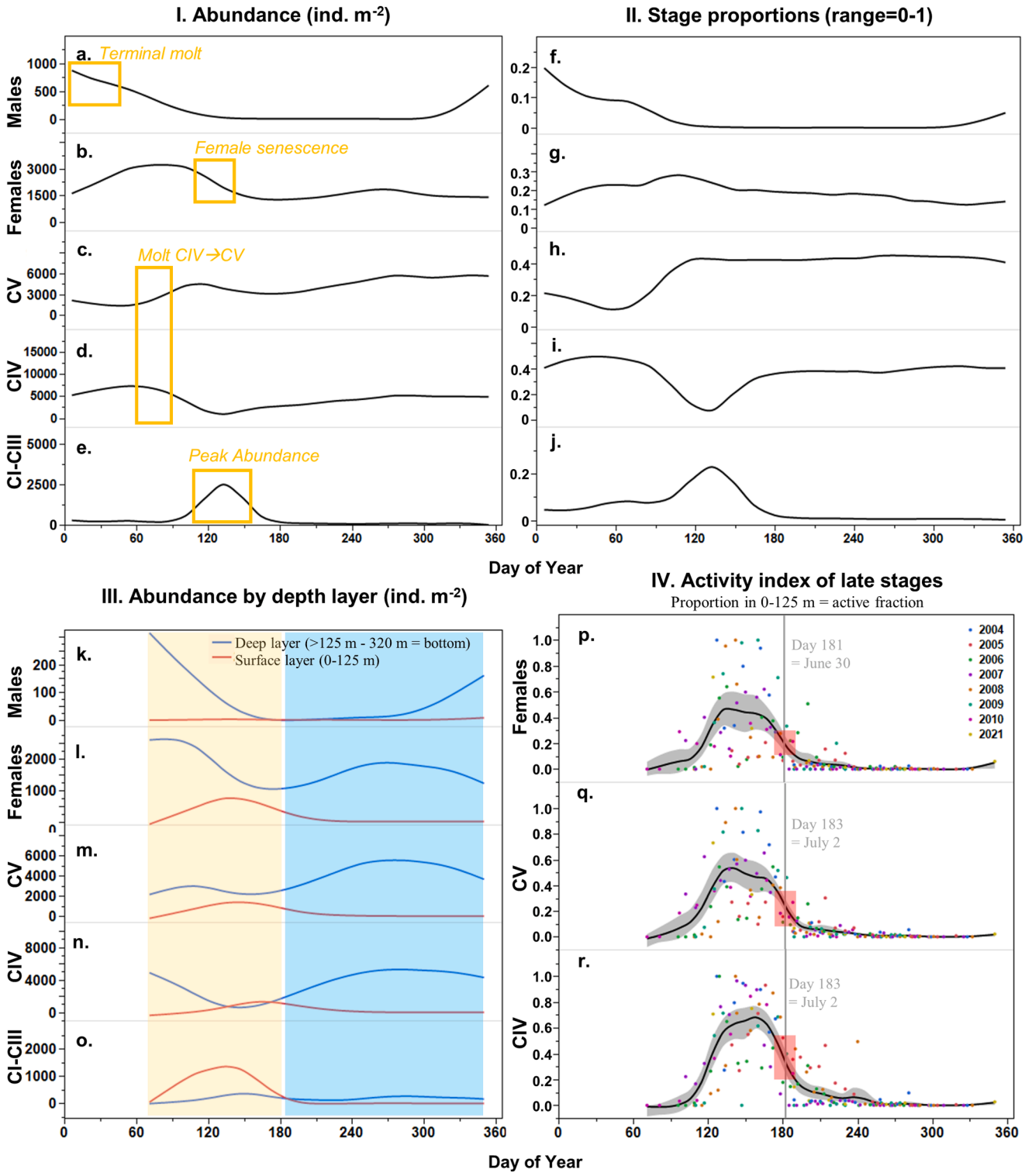

Fig. 2. Calanus hyperboreus phenology metrics are informed by the Atlantic Zone Monitoring Program (AZMP) climatological abundance. Climatological (1999–2021) stage-specific copepodite abundance (Panel I, ind. m^{-2}) and stage proportions (Panel II, %×0.01 with range = 0–1) are derived from vertically-integrated zooplankton sampling at the Anticosti Gyre and Gaspé Current stations, using a loess fit. Vertically-stratified abundance (Panel III; 2004–2010 and 2021) and the late-stage activity index (Panel IV, black line) are based on sampling at the Rimouski station. In Panel III, colored shading highlights the time periods corresponding to the active growth period ~ March-early July (yellow), and when late stages are mainly at depth in diapause ~ mid-July through the fall-winter (blue). The activity index (Panel IV, black line) is the loess fit to the stage proportion in the top 125 m of the 320 m water depth (dots = observed values, colored by year). Station locations are indicated on the Fig. 1 inset map, and additional details are provided in the text (Section 3.2).

a 79% maximum mean lipid content was reported (Schmid et al. 2018).

Size metrics used for model targets consider the pre-bloom and post-bloom dry weights of *C. hyperboreus* late stages (CIV, CV, CVI), which contrast the size differences between lipid-depleted individuals sampled near the end of the overwintering period, and the lipid-rich individuals sampled after the spring bloom and near the start of dormancy. In the LSLE, large increases in CIV-CVI mean dry weights coincided with the spring bloom onset, in contrast to no apparent growth trends during the pre-bloom period in April-May and the post-bloom period starting at the end of June (Plourde et al. 2003). We used these mean pre-bloom and post-bloom dry weights as targets without and with a significant lipid reserve: CIV∼300 vs 600 μg DW, CV∼700 vs 2100 μg DW, CVI∼1000 vs 3500 μg DW. These dry weight changes correspond to doubling, tripling, and a 3.5-fold increase for CIV, CV, and CVI respectively during the spring phytoplankton bloom (Plourde et al. 2003).

3.4. Reproduction and mortality

C. hyperboreus reproduction occurs at depth following the terminal molt during the overwintering period (Conover & Huntley 1991), in late autumn and winter based on location (Schultz et al. 2020), in advance of the spring bloom (Smith 1990). Males awaken early and inseminate the females, before dying relatively quickly (Hirche & Niehoff 1996, Hirche 1997), and therefore serve to indicate the terminal molt timing. In the GSL, the peak climatological abundance of males occurs in January-February, although males are present from December through April (<1% in April) (Fig. 2a,f). As capital breeders, newly molted females ($CVIF_{R1}$) convert a portion of the lipid reserve accumulated over the previous active season into gonads (Jónasdóttir 1999), and ultimately egg production (Conover 1967, Hirche & Niehoff 1996). Based on GSL egg production experiments, gonad maturation lasted ∼ 3 weeks at the population level (Plourde et al. 2003). The eggs, dominated by wax ester and positively buoyant, rise to the surface (Sømme 1934, Conover 1988, Conover & Huntley 1991, Jung-Madsen et al. 2013, Schultz et al. 2020). Egg size estimates range from 0.55 ug C (Conover 1967, Smith 1990) to 1.03 ug C (converted using 0.8 lipid carbon fraction, Schultz et al. 2020), while the egg carbon mass of 0.84 ug C (Plourde et al. 2003) was calculated for the LSLE after Huntley and Lopez (1992).

In GSL egg production experiments, females laid between 251 and 1585 eggs in total and produced 762 eggs on average (Plourde et al. 2003). The number of eggs produced was significantly related to the size of the female lipid reserve (Schultz et al. 2020), but in the study of Plourde et al. (2003), body size and fecundity were unrelated, although lipid content was not measured in the latter. In the GSL egg production experiments, mean daily egg production rates decreased from 11.9 eggs/female/day at 0 ℃ to 4.7 eggs/female/day at 8 ℃ (Plourde et al. 2003), but daily egg production did not vary significantly over the 0–6 ℃ range of temperatures in Schultz et al. (2020). Under increased experimental temperatures, egg lipid content remained constant and the duration of spawning shortened (Schultz et al. 2020), while both the spawning interval and clutch size declined in Plourde et al. (2003). It is challenging to compare egg production experiments involving different experimental temperatures and measurements (lipid content vs body carbon), but both studies point to a higher utilization of body C (lipid reserves) under warmer conditions, and less reserve available for egg production. In contrast, Conover (1962) found that for acclimated CV *C. hyperboreus*, warming from 2 to 8 ℃ does not result in significant respiration increases (Q10 ∼ 1).

Individuals are removed from the population through mortality. Zooplankton mortality is highly uncertain and depends on variable contributions from expiration or non-predatory mortality, such as senescence, disease, parasitism, and starvation mortality, and predation mortality incurred through interactions with visual and non-visual predators, whose guild composition, abundance and consumption rates vary in space and time. While non-predation mortality has been estimated to account for a quarter to a third of epi-pelagic zooplankton mortality globally (Hirst & Kiørboe 2002), the relative amount of predation mortality in the highly productive shelf ecosystem of the GSL could conceivably be greater. Temperature universally affects biological rates, and therefore is correlated with increased total mortality and predation mortality in the *meta*-analysis of Hirst & Kiørboe (2002).

In situ staged mortality estimates are not generally available for *C. hyperboreus*, although Arnkvaern et al. (2005) made estimates in a fjord in western Svalbard. Total mortality for the smaller congener *C. finmarchicus* in the Gulf of Maine was found to be strongly stage-structured (Ohman et al. 2002), highest for eggs, then late naupliar stages, and lowest for late copepodite stages(Ohman et al. 2002). A similar trend was described for *C. finmarchicus* early stages in the Labrador Sea, with mortality highest for eggs, intermediate for early nauplii, and lowest for late nauplii (Head et al. 2015).

In the northwest GSL, the local predator guild is comprised of carnivorous macrozooplankton, including euphasiids, hyperiid amphipods, mysids, chaetognaths, and jellyfish (Dufour & Ouellet 2007, Harvey & Devine 2009), and larval and juvenile planktivorous fish including capelin (Vesin et al. 1981, Savenkoff et al. 2007), while in the southern GSL, mackerel and herring (Runge et al. 1999, Darbyson et al. 2003), as well as North Atlantic right whales (*Eubalaena glacialis*) (Sorochan et al. 2019, Sorochan et al., 2023, Lehoux et al. 2020) target *C. hyperboreus* as prey. Cannibalism documented in egg production experiments (Hirche 2013, Jung-Madsen et al. 2013, Schultz et al. 2020) is likely minimal in nature, as the buoyant eggs ascend away from females at depth, which do not appear to feed during diapause and breeding (Conover 1962, Head & Harris 1985).

4. Model overview

We used a coupled bio-physical *C. hyperboreus* individual-based model (IBM) implemented in FORTRAN, with particle tracking and zooplankton model components (Chassé & Miller 2010, Benkort et al. 2020). Each particle represented a cohort of identical individuals, known as “super-individuals” (Miller et al. 1998, Maps et al. 2012a), with individual variability among particles in the assignment of randomly selected, uniformly distributed parameter values which describe diapause entry and exit in terms of individual lipid dynamics. Time independent biological model state variables included the particle ID number, birth date corresponding to when the egg clutch was spawned and assigned to a new particle, and a maternal ID number. Time-evolving state variables included stage (egg = 0 to adult = 12) which also tracks the molt cycle fraction (*i.e.*, stage 11.0 and 11.95 being a CV respectively at the beginning or the end of its developmental stage), body structural mass (ug C), lipid mass (ug C) for late stages with lipid sacs (≥CIII), activity state (active, diapause, reproduction in a gonad development or maturation phase, or an egg producing phase), a sex category that also informs female year, age (days), abundance (# identical individuals), and a suite of variables to track reproduction and lipid or mass metrics that relate to dormancy duration or starvation. Egg production was represented instantaneously (eggs/female/time step) and daily (eggs/female/day), and the model recorded the cumulative eggs produced during a female’s first- and second-reproduction pulses, and the spawn start and duration (days). Also tracked were the proportion of lipid catabolized since diapause entry (%) and the maximum structural mass achieved. *In situ* temperature and food concentration along the particle track were also recorded. Supplemental Fig. S1 diagrams the key *C. hyperboreus* population model state variables.

In the computation loop, vertical position was updated first for each particle, with particles advected vertically and then moving towards a preferred depth defined based on developmental stage and activity, using a biased, random walk formulation for vertical movement (Ornstein-Uhlenbeck equation; Uhlenbeck & Ornstein 1930, Gillespie 1996, Benkort et al. 2020). Since the model was implemented in 1-D, horizontal advection was not considered. Individual particles generally moved towards the preferred depth, but due to the random noise there is

Table 2
Model equations describing *C. hyperboreus* biology and behavior. The equations represent stage development and molting, respiration, ingestion and assimilation, growth and lipid accumulation, reproduction including gonad maturation and development and egg production, starvation, dormancy entry and exit thresholds, vertical displacement and mortality. References are indicated by superscript numbers for each category and sources are listed in the footnote. In the Appendix, see Table A1 for definition of state variables and parameters, and Table A2 for a complete definition of equation terms, references, and details on differences between this study and original formulations in Bandara et al. (2019).

Category	Equations
Development [2,4,7]	$D = a\_dev \cdot (T + 13.66)^{-2.05} \cdot f\_lim$, where $f\_lim = F^2/(k_{ft}^2 + F^2)$ $MCF(t) = MCF(t-1) + dt/D$
Molting [1]	Occurs if stage development suggests $MCF \geq 1$ & if $mass \geq molt\_crit$
Growth [1,7]	$G = aI - R - EP$
Starvation [1]	If $G<0$ and $lipid(t) \geq \lvert G \rvert$, then $lipid(t+1) = lipid(t) + G$ If $G<0$ and $lipid(t) < \lvert G \rvert$ or $lipid = 0$, then $mass(t+1) = mass(t) + G$
Lipid accumulation [1,7]	If $G>0$ and $stage \geq$ CIII: If $mass < 38$ µg C ind^{-1}, then $lipid = 0$; If $mass = 38$–159 µg C ind^{-1}, then lipid allocation rate increases exponentially from 0 to 0.65; If $mass > 159$ µg C ind^{-1}, then $lipid(t+1) = lipid(t) + 0.65 \cdot G$ Exceptions: CIII *lipid* capped at 10% DW as lipid; CIV-CVI *lipid* capped at 70% DW as lipid. Following terminal molt, CVIF can increase structural mass by up to 15%, after which CVIF allocate growth to lipid: $lipid(t+1) = lipid(t) + G$.
Ingestion [1,7]	$I_{REF} = 0.5 \cdot b \cdot M^m$ $I = I_{REF} \cdot c \cdot exp(n \cdot T) \cdot \frac{F^2}{k_f^2 + F^2}$
Respiration [1,7]	$R_{b\_ref} = 0.5 \cdot f \cdot (M+L)^o$ $R_b = R_{b\_ref} \cdot g \cdot \exp(p \cdot T)$ $R_a = 1.5 \cdot R_b$ $R_{active} = R_b + R_a$ $R_{dormant} = 0.25 \cdot R_b$ $R_{repro} = 0.62 \cdot R_b$
Gonad development & maturation [7]	3 week delay before spawning
Egg production [5,7]	$EP = 2 \cdot R_{repro}$ $lipid = lipid - EP$ If $lipid \leq lipid\_floor$, then EP ends. For $CVIF_{R1}$: $lipid\_floor = 0.15 \cdot max\_diap\_lipid$, For $CVIF_{R2}$ and $CVIF_S$: $lipid\_floor = 0$
Dormancy entry [1,7]	$lipid\_frac = lipid/(lipid + mass)$ If $stage \geq first\_diap\_stage$ & $lipid\_frac \geq d_{in}$ & $activity = 0$, then $flag\_enter\_diap = T$ For CIV-CV: If $flag\_enter\_diap = T$ & MCF ≥ 0.98 & $activity = 0$, then $activity = 1$ For CVIF: If $flag\_enter\_diap = T$ & $activity = 0$, then $counter\_c6\_active = counter\_c6\_active + dt$ If $counter\_c6\_active \geq 3$ weeks & $activity = 0$, then $activity = 1$ For all stages at entry into dormancy: $max\_diap\_lipid = lipid$
Dormancy exit [1,7]	$lipid\_frac\_burned = (max\_diap\_lipid - lipid)/max\_diap\_lipid$ if $lipid\_frac\_burned \geq d_{out}$, then $flag\_exit\_diap = T$ If $flag\_exit\_diap = T$, then: For CIV: $activity = 0$, $stage = 11.0$ For CV: $sex = 1$ (females), $abund = 0.8 \cdot abund$ (kill males), $stage = 12.0$, $mass\_limit = mass \cdot 1.15$, $activity = 2$ For CVIF: $activity = 2$
Vertical displacement [3,6]	OU biased random walk: $z(t+1) = rand \cdot sd + z_{opt} + (z(t) - z_{opt}) \cdot \exp(-theta \cdot dt)$ Where $rand$ = random number 0–1, and $sd = sigma \cdot sqrt(\frac{1 - \exp(-2 \cdot theta \cdot dt)}{2}{theta})$
Mortality [1,7]	M(total) = M(natural + predation) + M(starvation) + M(senescence) + M(death of males) where M(natural + predation) is: $m = I' \cdot (0.01 + m1 \cdot \exp(-m2 \cdot stage)) \cdot ((Tref + 13.66)^{-2.05})/((T + 13.66)^{-2.05}$ Visual predation scaling: $I' = ((max2 - min2)/(max1 - min1)) \cdot (L(z) - max1) + max2$ Light at depth: $L(z) = PAR_{surf} \cdot \exp(-k_d \cdot z)$ Dormant or reproducing: $m = 0.1 \cdot m$ Active CIV-CVI in September-December: $m = 2.25 \cdot m$ M(starvation) = $\min(1, 2 \cdot mass_{burn})$ *if* $0.1 < mass_{burn} \leq 0.5$, where $mass_{burn} = (mass\_max - mass)/mass\_max$ M(death of males) = Males killed at terminal molt: Abun(t + 1) = 0.8·Abun(t) M(senescence) = Spent females die after egg production: Abun(t + 1) = 0

Equation sources: 1. Bandara et al. (2019), 2. Bělehrádek (1935), 3. Benkort et al. (2020), 4. Ji et al. (2012), 5. Plourde et al. (2003), 6. Uhlenbeck and Ornstein (1930), 7. This study.

a spread around the preferred depth (S.D. ~6 m). Particles' effective vertical speed was assumed to be invariant with respect to size and stage. The preferred depth of eggs and non-feeding naupliar stages was 25 m, while feeding stages (≥NIII) sought the depth associated with temperature and food conditions in the upper 75 m that maximized their growth. Active late stages (CIII-CVI) experienced a 0.5 daily probability of performing diel vertical migration (DVM), which set the preferred depth to 100 m between sunrise and sunset. Next, the *in situ* temperature and food conditions were considered together with the individual's state in a set of biological equations governing stage development, ingestion, food assimilation, respiration, body structural growth and lipid accumulation, egg production, starvation, and mortality, as well as the transitions between active, diapausing and reproducing states. Based on these equations, the state variables (stage, age, structural mass, lipid mass, activity state, eggs produced, etc.) were updated. If an egg clutch was spawned, an empty particle was assigned to the location of the reproducing female and its maternal identification number was set to the female's identification number. The egg particle abundance was determined as # eggs/female × # females, structural mass was set to the egg mass constant, and other parameter values were inherited from the mother. Finally, at the end of the time step, the particle abundance was modified using the total mortality, which is the sum of the mortality incurred from starvation, senescence of second reproduction females following reproduction, the terminal molt to adult (all males killed for numerical efficiency), and a generic mortality that encompasses visual and non-visual predation and expiration mortality. This computation loop was repeated with the next time step (see summary in Fig. S1).

The model biological equations (Table 2) are based on Bandara et al. (2019), with modifications to simulate the observed patterns of growth, lipid accumulation and diapause timing of *C. hyperboreus* in the GSL. A full description of the biological model is presented in Appendix A, including a list of model state variables and parameters (Table A1) and the model biological equations for stage development, ingestion, food assimilation, respiration, growth, lipid accumulation and mobilization, catabolization of structural mass in the absence of lipid, diapause entry and exit based on lipid thresholds, egg production, and mortality (Table A2 and Appendix A.1-A.8). Portions of the model that deviate from Bandara et al. (2019) are detailed in the "Model Building" section below and summarized in Table A2. Emergent and prescribed model properties are listed in Table A3.

The IBM used output of the Gulf of St. Lawrence Biogeochemical Model (GSBM; Lavoie et al. 2021) for the year 2008. In this study, GSBM was forced with hourly surface forcing (air temperature, relative humidity, winds, cloud cover, and precipitation) provided by the National Centers for Environmental Prediction (NCEP) Climate Forecast System Version2 (CFSv2; Saha et al. 2010, Saha et al., 2014). A simulation was performed to obtain high-frequency output (2-hourly) for the physics (temperature, vertical velocities), while the biogeochemical output was every two days, and interpolated to every 2 h. GSBM has a horizontal resolution of 1/12th degree, and 46 vertical z-levels. The GSBM 2008 simulation was conducted using climatological boundary conditions as described in Lavoie et al. (2016), with the implication being that the post-2009 deep water warming observed in the GSL was not represented. In comparison to the observations, GSBM simulates the 0–6 m average temperature reasonably well, although the model surface layer is cooler than the CTD values in both mid-May and July-August 2008. Deeper in the water column, the model CIL temperature is very similar to observed, while the near bottom layer (248–295 m) mean temperature in the model (4.4 ± 0.17 ℃) is within 1 ℃ of the observed mean of 5.3 ℃. The simulated maximum chlorophyll-a concentration at the Anticosti Gyre station is very similar to satellite-based estimates for the northwest GSL in January-March, and captures the observed spring bloom onset timing and amplitude. In summer and early fall, the GSBM chlorophyll-a concentration is relatively high and variable like observed, but it is not as high as observed on average in the summer, and the observed fall bloom is not simulated by GSBM. The fall bloom missing from the GSBM forcing should not have a large effect on the simulated *C. hyperboreus* population, which is in dormancy at depth in July. Model food was the sum of GSBM small and large phytoplankton and microzooplankton. Light in the form of GSBM 4-hourly surface photosynthetically active radiation (PAR) informed visual predation mortality risk. 10-year long simulations were performed by repeating the year 2008 forcing. The GSBM 2008 temperature and food conditions in the northwest GSL are summarized in Fig. 3.

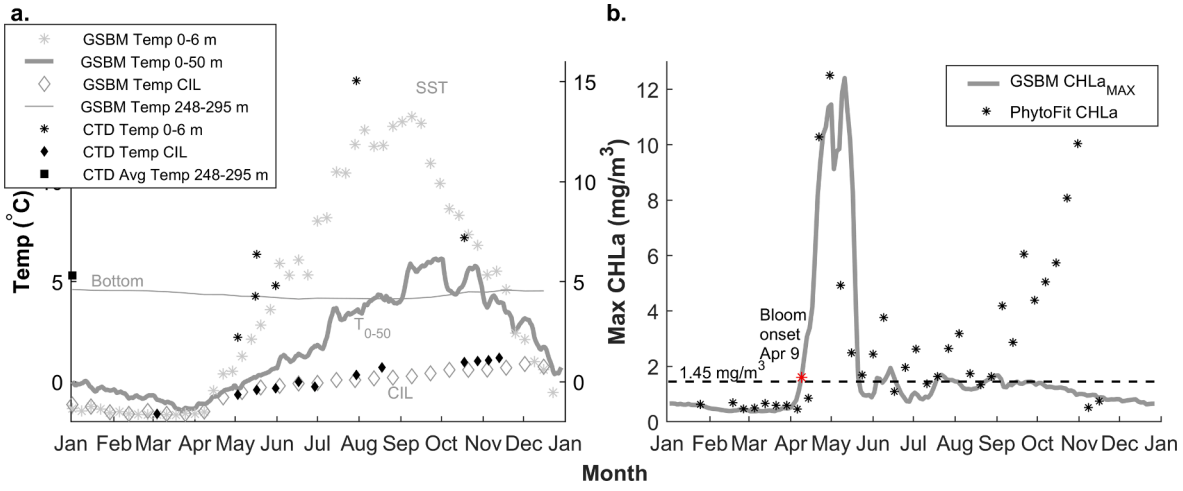

Fig. 3. Temperature and chlorophyll-a model forcing in 2008 simulated by the Gulf of St. Lawrence Biogeochemical Model (GSBM) at the Anticosti Gyre station in the northwest Gulf of St. Lawrence. a.) Daily model average temperature for the top 0–50 m (thick gray line), the top vertical level (0–6 m) which approximates sea surface temperature (SST, light gray stars; note every 14th daily value is plotted for improved visibility), the Cold Intermediate Layer (CIL, light gray diamonds) which is defined in the model as the coolest sub-surface vertical layer and the layer below, and the vertical level at 248–295 m which represents the bottom layer (thin gray line). For comparison, average temperatures from CTD casts collected in 2008 at AG (n = 12) are plotted for the top 0–6 m (black stars), the CIL which is defined as the 30 m depth layer extending down from the depth of the minimum temperature (black diamonds), and the 248–295 m layer, the latter as the annual average (black square on y-axis). b.) The daily maximum chlorophyll-a concentration in the upper 100 m, with a bloom onset date of April 9th (red star) based on when the maximum chlorophyll-a concentration first exceeds 1.45 mg m^{-3} (black dashed line). PhytoFit surface chlorophyll-a estimates derived from satellite 8-day composite images of the northwest GSL (black stars; Clay et al. 2021) are included for comparison.

Table 3
Summary of model building challenges encountered in early versions of the model and their exploration through sensitivity analysis. To simulate observed patterns of late-stage size and dormancy phenology, we had to address challenges related to individual energy dynamics, including food ingestion and assimilation, lipid accumulation, and respiration. The sensitivity analysis, performed with a combination of offline and online experiments, informed model building solutions which are described in the text. Note that the challenges of too high or too low lipid accumulation occurred under different model parameterizations: 30% vs 75% of net growth routed to lipid was respectively too low vs too high.

Challenge	Model Evidence	Sensitivity Analysis
Ingestion too high during pre-bloom (low food)	Females rapidly increased dry weight pre-bloom, and surpassed lipid threshold to enter dormancy	◂ Modify ingestion formulation from Type II to Type III, to decrease intake during lowest food concentrations; ◂ Vary the half-saturation coefficient of ingestion, k_f (0.15–0.55 ug C L^{-1}).
Assimilation too low during spring bloom (high food)	Late stages grow too little during bloom, and post-bloom dry weight lower than expected	◂ Vary assimilation coefficient of ingestion, a (0.60–0.87); ◂ Vary net growth routed to lipid vs structure (0.30–0.75).
Lipid accumulation too low	CIV and CV grow large bodied but lean, rarely triggering lipid threshold to enter dormancy	◂ Vary net growth routed to lipid vs structure (0.30–0.75).
Lipid accumulation too high	CIV developed small body structures with high fat content, enabling dormancy entry but they could not remain at depth for the expected duration of the overwintering period; Females were small-bodied with low DW.	◂ Vary net growth routed to lipid vs structure (0.30–0.75); ◂ Limit CIII lipid accumulation to 10% of DW; ◂ Slow development under low food with Type III response, to increase body structural growth.
Dormancy respiration too high; Range of lipid thresholds triggering entry too low for stages preparing to reproduce; Range triggering exit too high for stage CIV	Dormancy duration was shorter than expected, especially for CIV; Also, late-stage dry weights were lower than expected.	◂ Vary respiration mass coefficient (f) for all development stages (−5% to −20%), and for dormant CIV (further −10% to −30%); ◂ Vary range of lipid thresholds (d_{in}, d_{out}) to allow greater drawdown of lipid reserve for CIV, and higher lipid proportions to enter dormancy for stages preparing to reproduce.

4.1. Model building: Improving the *C. hyperboreus* biological model

In order to simulate observed patterns of *C. hyperboreus* growth and dormancy in the GSL, it was necessary to modify some aspects of the biological equations and parameters inherited from Bandara et al. (2019; referred to as B19 in this section). Below we describe the modelling challenges encountered with respect to individual size and phenology, the sensitivity analysis used to explore the characterization of the biological process, and the model modifications that were implemented. The modelling challenges and sensitivity analysis are summarized in Table 3. In the Discussion, we interpret how these model choices affected the population structure and the individual life histories and discuss what this teaches us about the *C. hyperboreus* population in the GSL.

4.1.1. Copepod size

Achieving a realistic individual size at stage required balancing rapid growth during the spring bloom with the observation of little growth while food is low under pre-bloom conditions. A combination of offline and online sensitivity analyses were used to explore the evolution of individual structural mass and lipid mass under different assumptions about ingestion, respiration, and lipid accumulation (not shown, see summary in Table 3). The following challenges emerged from early simulations performed under varied model parameterization and equations: (i) females developed large lipid reserves before the spring bloom, while food was low, contrary to observations, (ii) females that did not grow sufficiently during the spring bloom to reach their expected large DW despite high food availability, (iii) CIV and CV individuals grew a large structural mass but did not become fat enough during the spring bloom to trigger diapause entry, (iv) CIV that accumulated a large proportion of lipid but had a smaller than expected structural mass, together with females of low DW, and (v) dormancy duration that was shorter than observed, especially for CIV. Therefore, we implemented changes in ingestion and development functions (detailed below), along with adjusting the rates of food assimilation, lipid allocation, and respiration within ranges supported by observations reported in the literature.

We reduced ingestion during low food conditions by implementing a sigmoidal response curve (Type III, Holling 1965), and selected the half saturation coefficient of 27 μg C L^{-1} to align with the pre-bloom food levels in the GBSM forcing. Development rate was also reduced during low food conditions, to allow CIV enough opportunity to accumulate lipid, again using a sigmoidal response but here the half-saturation coefficient was set to 10 μg C L^{-1} corresponding to the background concentration of microzooplankton pre-bloom. This allowed CIV to build sufficient lipid during the bloom before molting to stage CV. Experimental estimates of *C. hyperboreus* female food assimilation under varying food levels and ingestion rates reported a range of 84.2–87.7% (Tande & Slagstad 1985). Therefore, we increased the food assimilation rate from 60% used in B19 to the experimental mean of 86.4%. This modification allowed late stages to grow as large as observed over the course of the spring bloom. Since growth is the balance of assimilation and respiration, a 10% reduction in the linear coefficient of mass for respiration (f) also affected individual growth trajectories, enabling higher growth. 65% of net growth was allocated to the lipid reserve, which was found to balance the structural growth with the accumulation of lipid. We increased the maximum lipid content of late stages from 41% used in B19 to 70% to simulate observed DW and lipid content values. Since stage CIII develops an lipid sac but does not overwinter in the GSL, it was capped at 10% of DW as lipid. Finally, we allowed new females to increase their structural mass by up to 15% relative to their final stage CV mass, to represent the terminal molt size increase. After achieving the 15% large body structure, growth was entirely allocated to the lipid store.

4.1.2. Phenology

Achieving the appropriate mass and lipid content, as described above, typically improved the ability of the model to simulate the observed phenology of *C. hyperboreus* in the GSL. However, we made additional modifications to further improve model performance relative to the observed timing of life history events, including dormancy entry (late June-early July), molt to adult (January-March), peak egg production (January-March), CIV-CV molt and dormancy exit (March), and the timing of early stages (CI-CIII) peak abundance coincident with the spring bloom (April), as shown in Fig. 2. We adjusted the model lipid thresholds for diapause entry and exit, to allow CIV entry to diapause at a lower lipid fraction than CV and CVI (33–40% for CIV vs 41–47% for CV-CVI), and greater drawdown of lipid before triggering diapause exit for CIV (75–95% for CIV vs 44–64% for CV-CVI). Since CIV is not preparing to reproduce at the end of the overwintering period, it may have lower metabolic requirements in dormancy. Overwintering stage CIV basal respiration was therefore reduced by 25% in order to simulate a sufficiently long dormancy duration and the observed timing of molt to

CV and return to the surface in March. We explicitly model two reproductive phases, (i) gonad development and maturation, and (ii) egg production. The gonad development and maturation phase was specified to last three weeks based on egg production experiments in the GSL where the ~3-week time lag between 0% and 50% mature females corresponded to the timing when egg production rate exceeded non-negligible levels (i.e., >5–7 eggs/fem/day) (Plourde et al. 2003). This first reproductive phase of gonad development and maturation effectively delays the timing of egg release by 3 weeks.

4.1.3. Abundance and mortality

Modifications to mortality were implemented to achieve a quasi-stable abundance over the 10-year simulation and avoid population crashes or explosions. Mortality was restructured from B19 to reproduce the observed pattern of a total temperature-dependent mortality that decreases with stage (Ohman et al. 2002, Ohman et al., 2004), while still accounting for visual predation mortality in a simplified form. Following Maps et al. (2012a), mortality rate decreases with increasing stage such that eggs have highest mortality losses, followed by young nauplii (*etc.*), with a weak temperature dependence. We follow the assumption in B19 that higher mortality occurs under higher light availability at the particle depth, due to increased visual detection and predation. In our model, light at depth is determined from GSBM surface photosynthetically available radiation (PAR_{surf}) and a constant light attenuation coefficient ($k_d = 0.06\ m^{-1}$), and the highest light inflicts a 50% increase in total mortality. Additionally, mortality is increased 2.25-fold for late stages remaining in the near surface layer in the fall (September-December), when observations suggest the entire population should be at depth. Initial particle abundance and mortality parameters were adjusted to ensure sufficient survival of early feeding stages and avoid a population crash. A visualization of how mortality varies for various stages with season and depth is included in the Supplemental (Fig. S2, Fig. S3).

4.2. Model initialization and experiments

We initialized the model in the northwest GSL with 24 particles each representing a cohort of 25,000 new eggs on January 3, 2008 and provided as input a "paramosome" vector populated with most of the individual's parameter values (Record et al. 2010, Maps et al. 2012b). Dormancy threshold parameters d_{in} and d_{out} were instead randomly sampled from distributions within the model, providing interindividual variability. A large number of inactive, empty particles were stored in a 'waiting room' pending the release of a new clutch of eggs, once the initial cohorts develop to females and begin egg production (as described in Section 4.0). Due to computational limitations associated with performing 10-year long runs, the number of initial particles was selected to be high enough to include sufficient individual variability (24~30, the population size typically required to make assumptions about normally distributed properties), and low enough such that after 10 years the model has not run out of empty particles, which avoids a crash.

In the baseline simulation, a 10-year simulation was performed under GSBM 2008 repeat year forcing. The baseline simulation used a diapause strategy that allows CIV as the first stage to enter diapause and includes second-year females. This 10-year run was sufficiently long such that the initial cohort develops into second reproduction females with a final reproductive pulse at ~3 years. The eggs released by those spent $CVIF_{R2}$ reached the adult stage, reproduced, and achieved the final egg production event at ~6 years. Those offspring did the same to ~9 years, with the result that 3.3 generations were completed. In the case where CIV did not accumulate sufficient lipid to trigger diapause entry, entry was delayed and occurred during stage CV. The CV-first diapause pathway resulted in a life cycle one year shorter, increasing the number of generations (~5) realized over the 10-year simulation period. While the first dormancy stage is driven by CIV-CV accumulating lipid in excess of the threshold lipid content for the current stage, the presence vs absence of second reproduction females was selected *a priori* in the model input. One additional simulation was therefore performed without the second reproduction female strategy to evaluate the effect of iteroparous females on the simulated population.

5. Results

5.1. Simulating a quasi-stable C. hyperboreus population structure in the northwest GSL

The model simulated a relatively stable population structure over the seasonal cycle that was generally similar to observed patterns in the northwest GSL. The population stage structure produced a consistent seasonal pattern in the proportions of various development stages after the first 5 years of the simulation (Fig. 4a). Peak egg production lasted 2.5–3 months during January – March, and the tails of egg production extended from early December through April (Fig. 4b). The timing of peak egg production aligned with the "target" values from Table 1. The peak abundance of early copepodite stages (CI-CIII) occurred during the spring bloom (Fig. 4a-b), consistent with the observed climatological pattern in the lower Estuary (Blais et al. 2021). A portion of the new generation (G0) entered diapause as stage CIV in the first three weeks of June, while the remaining active G0 individuals develop to CV before entering diapause (Fig. 4a-b). The overwintering population was composed of stages CIV, CV, and CVI. The relative stage abundance in dormancy was stable, here as mainly CV (~60%), and CIV and CVI contributing ~20% each (Fig. 4a). This simulated overwintering population structure was within the range observed in the LSLE, where low CIV contributions (~15–20%) were reported in 1994 and 1997, and during the latter year CV comprised ~60% (Plourde et al. 2003).

The maximum annual CI-CVI abundance decreased through the first year since females have yet to reproduce, and subsequently increased from the second year onward, with an increasing number of eggs produced each year (Fig. 4b, see supplemental Fig. S4 for years 1–7). From year 2 onward, the maximum CI-CVI abundance increased by about 10% per year. Since the model was designed to represent the population structure, a simplistic mortality formulation was adjusted to allow the initial cohort to survive the multi-year spin-up period while developing from egg through adult, and to avoid subsequent population extreme events, such as crashes or explosions. The small trend in abundance was therefore expected based on the choice to not prioritize population closure.

The model predicted realistic seasonal patterns in the mean dry weight (μg C, DW=structural C mass + lipid C mass) and lipid mass of late stages, with the timing of peak DW and lipid mass (μg C) corresponding to diapause onset (Fig. 5a,b). During the pre-bloom period (<April 12th in year 2008 forcing), DW remained low or increased slowly (Fig. 5a). In contrast, large increases in DW and lipid were simulated during the spring bloom (Fig. 5a,b). During dormancy, the simulated mean lipid mass slowly decreased as lipids were catabolized (Fig. 5b). Since $CVIF_{R1}$ molt from CV at depth and do not feed, the mean dry weight of $CVIF_{R1}$ was below that of CV in November-January. The decline in the mean CV DW between dormancy onset and the spring bloom is driven by lipid utilization during dormancy, and accelerates in the beginning of January reflecting the addition of smaller, recently-molted CVs.

Time series are plotted along each particle's track every two days for (a, b) *in situ* temperature (℃, black) and total food concentration (μg C/L, green, right y-axis), (c, d) depth (m) and activity state (by color, see legend), and (e, f) the evolution of dry weight (μg C/ind., thick black line), structural mass (μg C/ind., gray line), lipid (μg C/ind., gray dash), and egg production (# eggs/female/day × 100, pink line). Also, the timing of egg spawning (pink circle) and select stage molts to stage NIV, CIV, CV, and female (red 'x') are plotted on the mass trajectory. The particle exhibiting the CIV-first diapause phenotype (left) was spawned

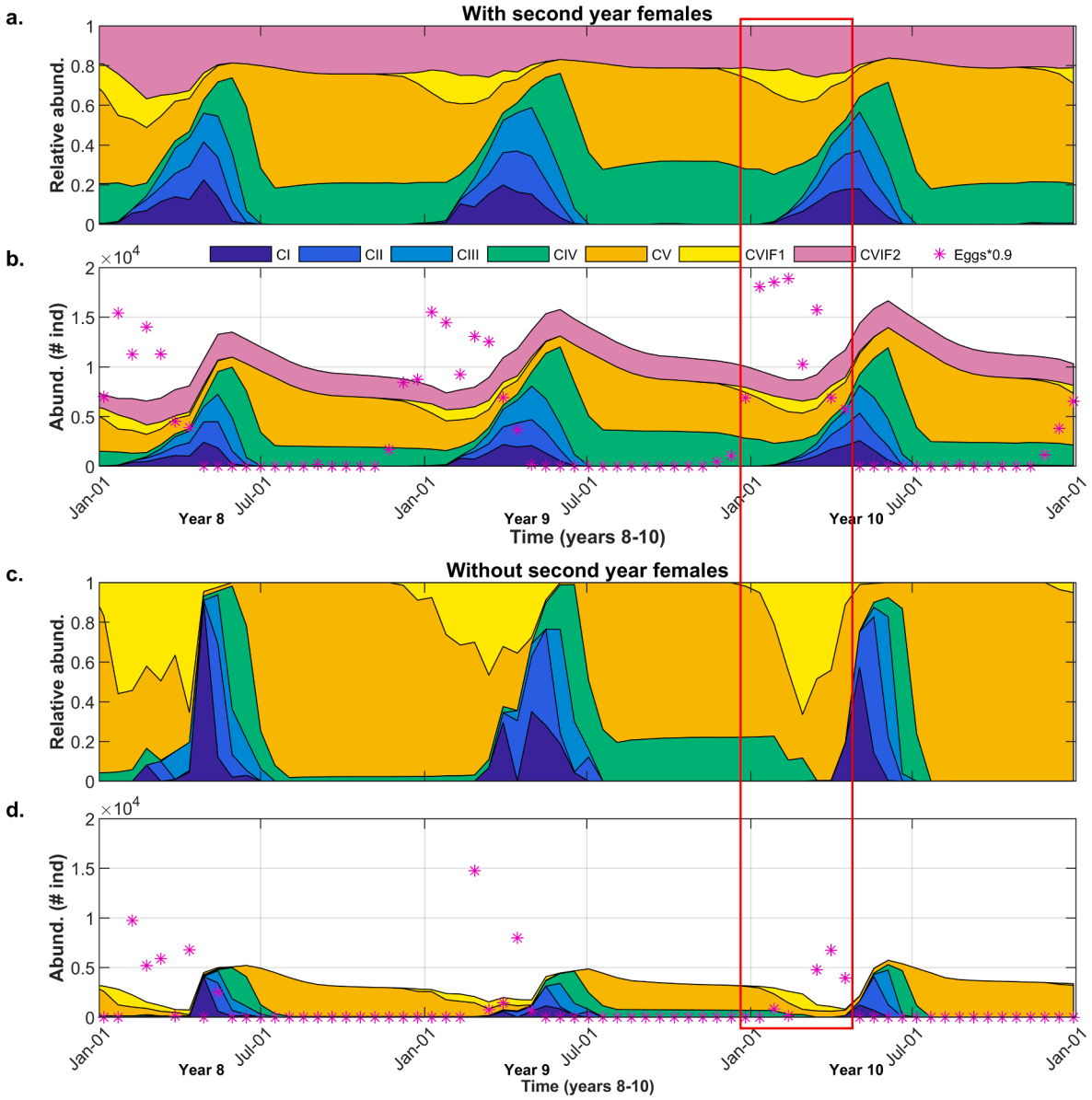

Fig. 4. Simulated *C. hyperboreus* population structure at Anticosti Gyre station over the last 3 years of the 10-year simulation, using repeated 2008 environmental forcing. The time evolution of the population, plotted biweekly, includes the (a) population stage structure, based on stage fractions of the total CI-CVI abundance, and (b) abundance of copepodite stages CI-CVI, including first year and second year females (CVIF1 = yellow, CVIF2 = pink), shown with egg abundance scaled by 0.9 (pink stars). (c)-(d) are as (a)-(b), but show results from the simulation excluding second reproduction females. The red box highlights the time period of peak egg production in the baseline simulation during Year 10. Note that the complete 10-year time series, and the naupliar abundance, are included in the Supplement (Fig. S4).

in mid-December of year 6, and entered diapause at stage CIV in mid-June. The particle exhibiting the CV-first diapause phenotype (right) was spawned in late March, and developed to stage CV before entering diapause in late August.

Late-stage DW varied seasonally with the timing of the active growth, overwintering periods, and spawning in the case of females. Maximum DW coincided with the end of the active growth period and entry into dormancy for each year (Fig. 6). For overwintering late stages, minimum DW occurred just before the exit from dormancy for CIV, or at the end of female egg production (Fig. 5b, 6c-f). When females released eggs, the lipid carbon was drawn down, as seen in the individual body size trajectories (Fig. 6e,f). On average, second reproduction females spawned for 3 weeks, producing 173 eggs (range 104–278) at a production rate of 7.45 eggs/female/day (see Fig. 6e,f pink lines). First reproduction females had lower fecundity (mean 76.2 eggs, range 34–118 eggs), lower daily production (mean 6.68 eggs/female/day), and a shorter spawning duration (mean 10.3 days). Late-stage growth was generally maximized during the high food conditions of the spring bloom (Fig. 6a-b,e-f), but CV developing post-bloom also achieved high growth rates in the model (Fig. 6b,f). For stage CV, a local minimum DW occurred in February-March, coinciding with lipid-depleted CIV molting to CV, and the few remaining overwintering CVs with low lipid reserves (Fig. 5, Fig. 6e,f). We calculated the simulated pre-bloom and post-bloom DW frequency for each late stage in carbon units and mass units from the final year of the simulation by converting the dry weight frequency distribution from units of μg C to μg after assuming late stages are 60% carbon (Smith 1988): the mean DW (μg) pre-bloom/post-bloom is 504/924 for stage CIV, 1470/2177 for stage CV, and 1810/2755 for $CVIF_{R2}$ (Fig. 7). Compared to the DW observed in the LSLE pre-bloom and post-bloom by Plourde et al. (2003; see Table 1), the simulated DWs are larger for CIV during both time periods, similar for CV when considering pre-bloom model values <1000 μg from that bimodal

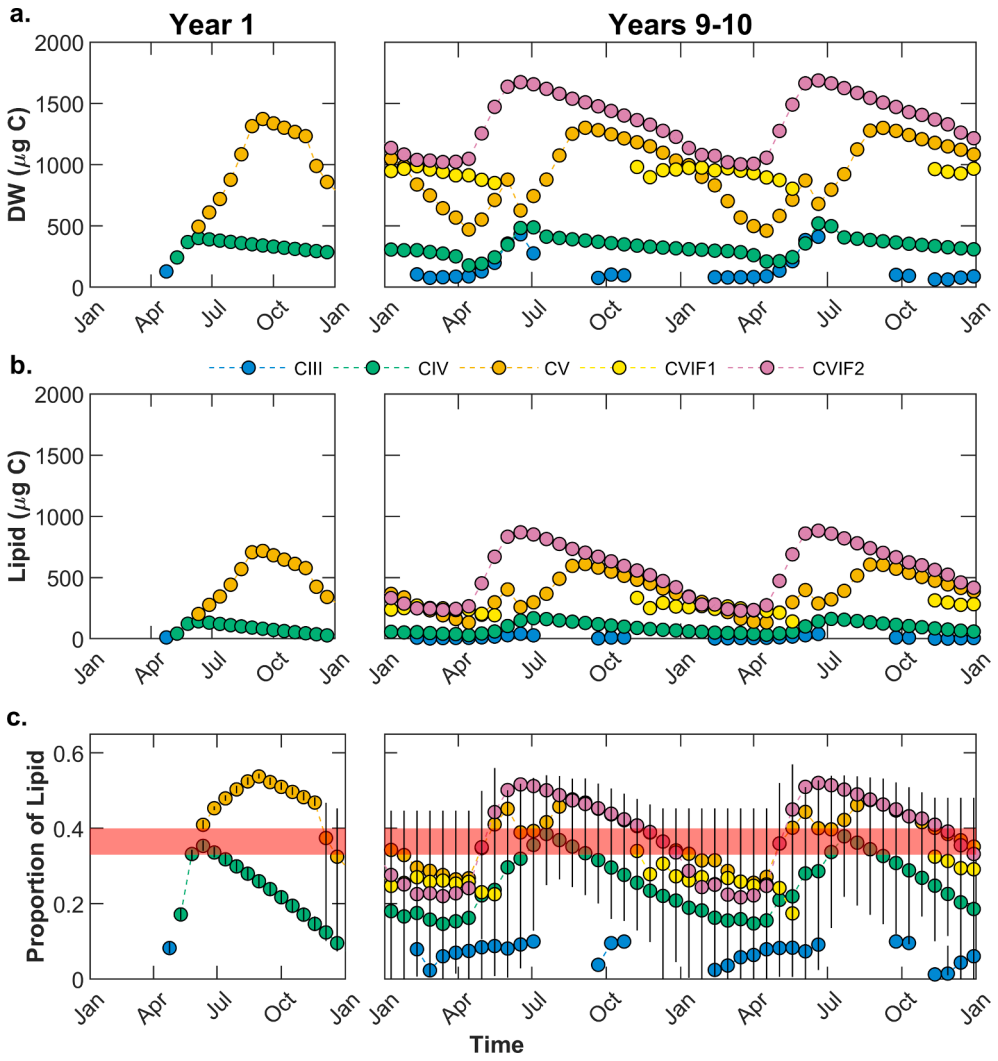

Fig. 5. Seasonal cycle of *C. hyperboreus* growth and lipid accumulation simulated for stages containing lipid sacs (CIII-CVI) in the northwest GSL. Biweekly time series plot the abundance weighted mean values by stage for (a) dry weight (μg C/ind.), (b) lipid mass (μg C/ind.), and (c) proportion of dry weight as lipid (lipid fraction, range 0–1; vertical bars indicate total range). For stage CIV, the lipid threshold triggering diapause entry is drawn from the parameter range 0.33–0.40 (red shading). A higher range of 0.41–0.47 is used for stages CV-CVI (not shown). CVI are classified as first and second reproduction females, defined based on the time period from the terminal molt through first reproduction (= $CVIF_{R1}$), and from the ascension to the active layer through the final reproduction (= $CVIF_{R2}$). Colors as in Fig. 4.

distribution, and simulated $CVIF_{R2}$ are larger than observed pre-bloom, but smaller post-bloom. The active season mean DW changes correspond to ~doubling for stage CIV (×1.8), ~tripling for stage CV if we consider only values <1000 μg from the pre-bloom bimodal distribution, and a 1.5-fold increase for $CVIF_{R2}$.

Dormancy entry timing was simulated fairly well by the model following the spin-up period, with the 50th percentile of each stage entering dormancy within 5 weeks of the target of early July (Fig. 8, Table 1). Second reproduction females typically entered dormancy the earliest in the model, and ~80% entered between mid-May and mid-June (50th percentile is last week of May). Simulated CIVs entered dormancy during the first three weeks of June (50th percentile is mid-June), which corresponds to the model target. CV entry into dormancy occurred over a broad time period and was shifted later than observed in the model. A small early cohort of CV (<20%) entered dormancy in June and July, but most entered in August (50th percentile is mid-August). Up to one-fifth of CVs entered dormancy in September. Upon inspection, we found that the CVs entering dormancy in June-July (target timing) were those that overwintered as stage CIV, and molted to CV that spring. By contrast, the CVs entering diapause from August onward had actively developed from eggs (G0). These timing differences for G0 and G1 CVs are also visible in the simulated life history trajectories (Fig. 6e-f).

Dormancy exit was simulated close to the target timing for each stage but occurred over a wider time window in the model (November-May). Specifically for CV molting to female at depth and females, dormancy exit timing corresponds to the end of reproduction via gonad development and maturation, hence not a true "exit" which is often associated with molting to the next stages and ontogenetic vertical migration to the surface such as in the transition between CIV and CV (see below). Second reproduction females exited first (~November-February), CVs that molt to first reproduction females generally exited in mid-December-March, and CIVs molting to CV exited dormancy in December-May (Fig. 3a, Fig. S3). Following the spin-up period, CIVs molted to CV and returned to the surface mostly from December through March, with small percentages exiting in April (~5%) and May (<5%, Fig. S3g). CVs molted to adult mainly from December through February, with a small fraction in March (~10–15%) and April (2–3%) (Fig. S3h). Females began gonad maturation primarily in December (40%), although the distribution of this timing extended from November (~15%), through January (~23%) and February (~17%), and a small tail of <5% in March (Fig. S3i). Since gonad maturation and development were simulated as a constant three-week period, followed by egg laying at depth, the average depth of females shallowed starting in January, when females who completed reproduction ascended to the surface active

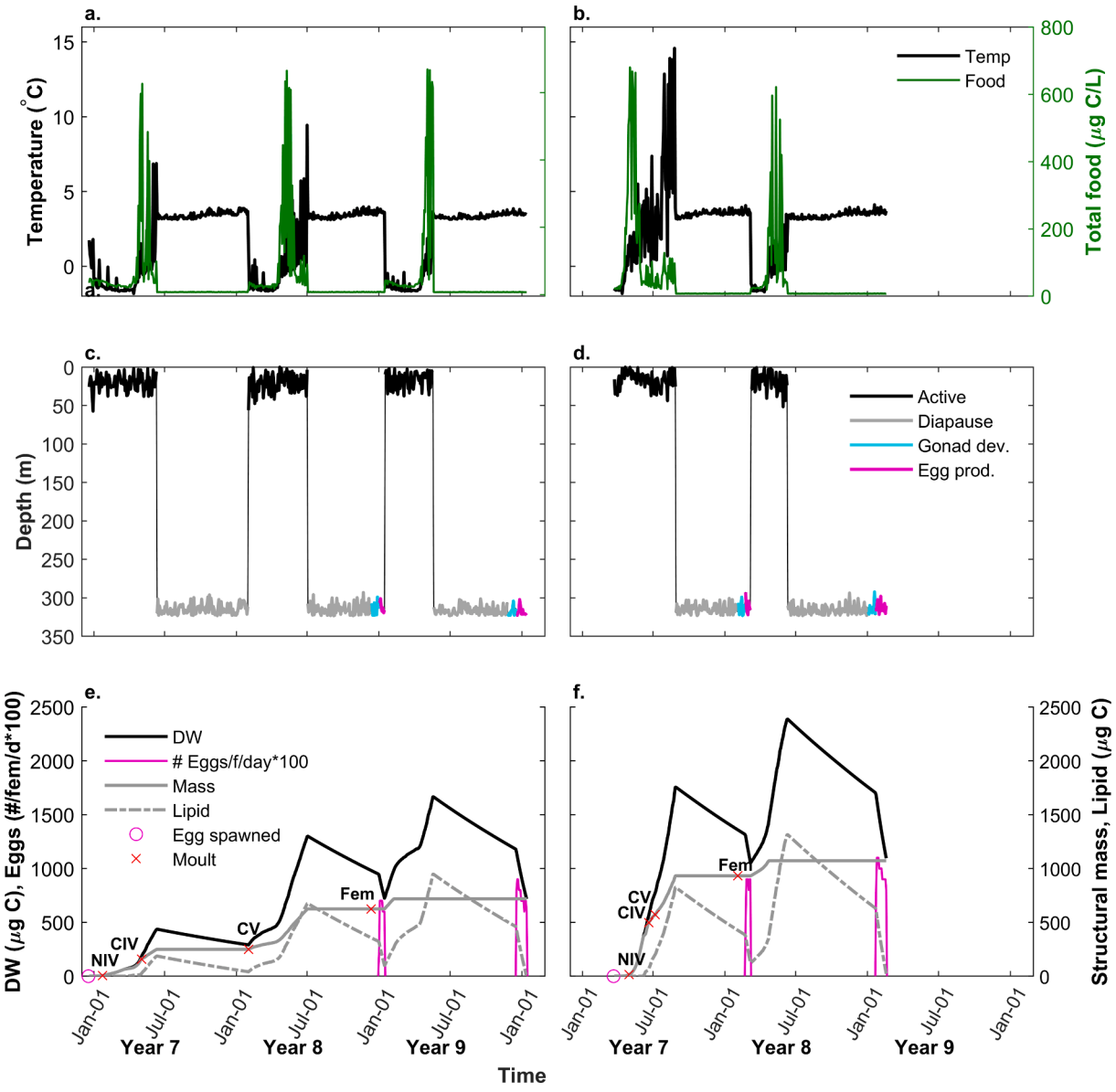

Fig. 6. Simulated life history "trajectories" for two particles with contrasting diapause phenotypes, CIV-first with a 3-year life cycle (left) vs CV-first with a 2-year life cycle (right).

layer (Fig. S3l).

5.2. *Simulated population responses in the absence of iteroparity*

Without second reproduction females, the model simulated a quasi-stable population structure dominated by CVs during the overwintering period (Fig. 4c), but lower egg production resulted in lower abundance than the baseline simulation (Fig. 4d). In the absence of iteroparity, the life cycle duration decreased from 2-3 years to 1–2 years. A small fraction of the new generation entered dormancy as stage CIV (~1–20% of the overwintering population). Comparing years 8–10, the seasonal pattern of egg production changed from a wide flat window of maximum egg production lasting ~8–10 weeks in the baseline simulation to a sharper peak of 2–6 weeks of maximum egg production. Total egg production was also reduced without second reproduction females, and the population contracted to $<0.6 \times 10^4$ peak CI-CVI abundance in year 10, in comparison to 1.6×10^4 in the baseline simulation (Fig. 4b,d).

Several life history phenotypes were simulated by the model, with both stage CIV and CV predicted as the first dormancy stage, which we refer to as "CIV-first" and "CV-first" dormancy phenotypes (see life history trajectories in Fig. 6), and reproduction in second year females switched on ("iteroparity", with successive reproduction termed R1 and R2) in the baseline simulation or off ("semelparity" = S). Approximately a third of the new generation (G0) entered diapause as CIV-first in the seventh year of the baseline simulation. Without iteroparity, the CIV-first fraction of G0 was reduced to 4% in year 7 (range 1–20% across years). The average size of the CV-first dormancy phenotype was larger at the beginning of reproduction than the CIV-first phenotype, with higher C dry weight (Fig. 9a, bars). Iteroparous second reproduction females were significantly larger than the semelparous females at the start of reproduction (R2 vs S). Semelparous females were similar in size to the iteroparous first reproduction females with the CV-first phenotype, but smaller than those with the CIV-first phenotype (S vs R1). Similar size differences were found at the start of dormancy, when females achieved their maximum DW preceding the reproduction (Fig. 9a, red triangles). Associated with their high lipid content, the second reproduction females produced the most eggs on average during spawning (Fig. 9b, R2), with 147 and 183 eggs/female, respectively, for CIV-first and CV-first phenotypes. Iteroparous first reproduction females were approximately half as productive during their spawn (R1).

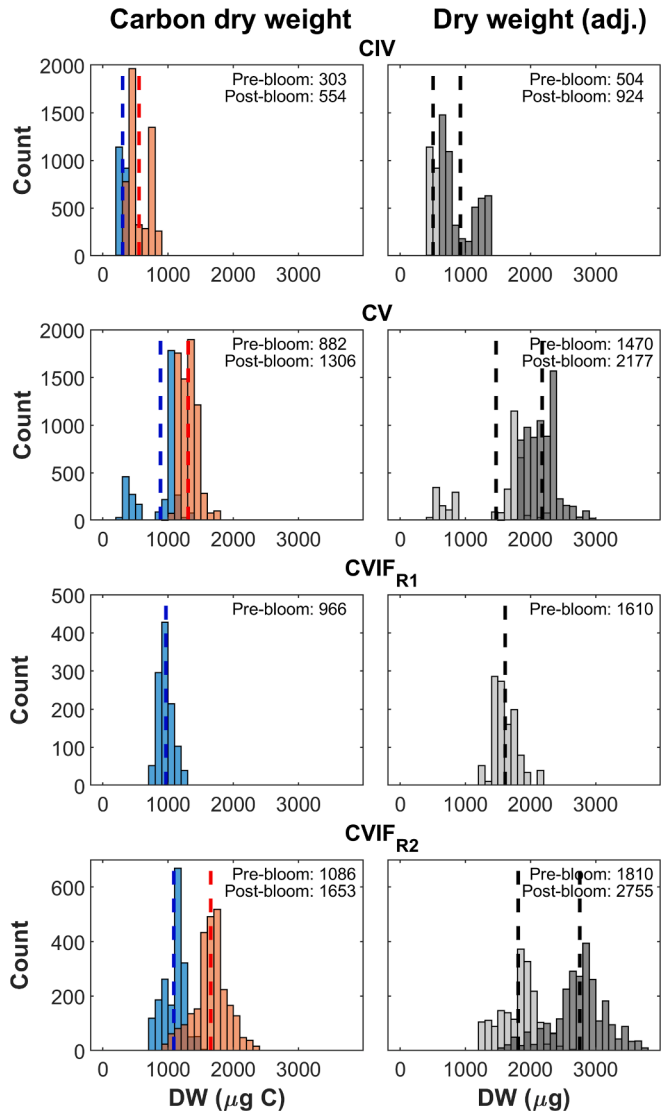

Fig. 7. Frequency distribution of model pre-bloom and post-bloom dry weight for late stages in the final year of the baseline simulation (Year 10). Size is represented in the model units of μg C (left, colored), and converted into mass units of μg by assuming a 60% body carbon content (right, grayscale) for each stage (CIV=top row, CV=second row, first reproduction females = third row, second reproduction females = bottom row). The pre-bloom staged dry weight (blue, light gray) is determined by sampling the model in early February. The post-bloom dry weight (red, dark gray) is sampled in early July for CIV, early June for females, and early September for CV, to characterize each stage closest to their entry into dormancy.

Utilizing the entire lipid reserve, semelparous females (S) spawned ~one-third more eggs than the iteroparous first reproduction females (R1), but over the course of a lifetime, semelparous females produced less than half of what iteroparous females produced (S vs R1 + R2: 101 vs 221 eggs/female for CIV-first and 110 vs 260 eggs/female for CV-first). At the population level, the CV-first dormancy phenotype contributed an order of magnitude more eggs due to its higher relative abundance, producing 221,000 during R1 and 322,000 eggs during R2 while the CIV-first dormancy phenotype produced 46,000 eggs during R1 and 50,000 eggs during R2, for a total of 639,000 for both phenotypes and years (not shown; eggs rounded to thousands). Without second reproduction females, the new generation (G0) entering dormancy was one third less abundant, and the total number of eggs produced dropped to 275,000 for both phenotypes combined. With iteroparity, egg production started over a wider window for the CV-first phenotype (Fig. 9c, R1 + R2 vs S), while the small number of particles in the CIV-first semelparous simulation (n = 2) prevents comparing the timing variability. Second reproduction females also began spawning over a longer time range than first reproduction females, and in the case of CV-first dormancy phenotypes, a median start timing that was several weeks earlier (R2 vs R1).

6. Discussion

This paper presented a new individual-based model of *C. hyperboreus* population dynamics, which included free-evolving lipid dynamics and lipid-triggered dormancy transitions, and which was able to simulate life cycle "targets" for the northwest GSL. Below we highlight several model modifications that were required to simulate the GSL size and phenology targets, and what we learned about key biological processes for the species through that process. In particular, we examine the hypothesized role of second reproduction females in *C. hyperboreus* population structure and growth.

6.1. Model performance

Our model is the first to simulate the full *C. hyperboreus* life cycle in the northwest Atlantic. By combining free-evolving individual lipid mass with a mechanistic description of dormancy entry and exit (*i.e.*, lipid-based triggers), the model simulates both the *C. hyperboreus* individual size trajectories and timing of key life history transitions (*i.e.*, dormancy entry and exit, egg production). This is in contrast to previous *C. hyperboreus* population models which either calculated lipid mass but specified diapause entry timing (Aarflot et al. 2022), or used a mechanistic description of diapause entry and exit in conjunction with a lipid content that was not fully free-evolving (Bandara et al. 2019). Our improvements to existing models include the tuning of a handful of model parameters and functional forms (*e.g.*, food-limitation on ingestion and development rate) that revealed key processes that were essential to produce an emerging population structure similar to what is observed in the GSL.

The initial numeric population of egg particles converged rapidly towards the observed overwintering population stage composition (CIV-$CVIF_{R2}$). The simulated dormancy duration, the timing of egg production, exit from dormancy, and peak CI-CIII abundance also align with observed phenology. However, while the dormancy entry is close to the early July target for stage CIV and females, most stage CV tends to enter dormancy later than observed. This is likely due to the complex interplay between the processes regulating development and the allocation of energy gained through feeding, which depends on both food availability and temperature. The simulated size distribution of late stages (CIV-CVI) near their entry into dormancy convincingly overlaps with the observed post-bloom size distribution. In the model though, females do not reach the higher end of the size distribution, nor do they achieve the highest fecundity estimated during egg production experiments in the region (Plourde et al. 2003). These discrepancies may result from transport from upstream regions and differences in bloom conditions. The LSLE has high chlorophyll concentrations half of the year (Lavoie et al. 2021) and experiences a later, larger magnitude bloom than the northwest GSL where we located our 1-D numerical experiment (Laliberté & Larouche 2023). As a result, a large proportion of the *C. hyperboreus* population initially developing in the estuary is flushed towards the northwest GSL throughout summer, and the origin and growth history of females sampled in late summer-fall are unclear. Model limitations related to the 1-D configuration, visual predation mortality, and the assumption of the CIV-first dormancy stage are discussed in Section 6.4.

6.2. Identifying key C. hyperboreus processes through modelling

In early simulations exploring how structural mass and lipid mass evolve in response to model parameters and equations (summarized in

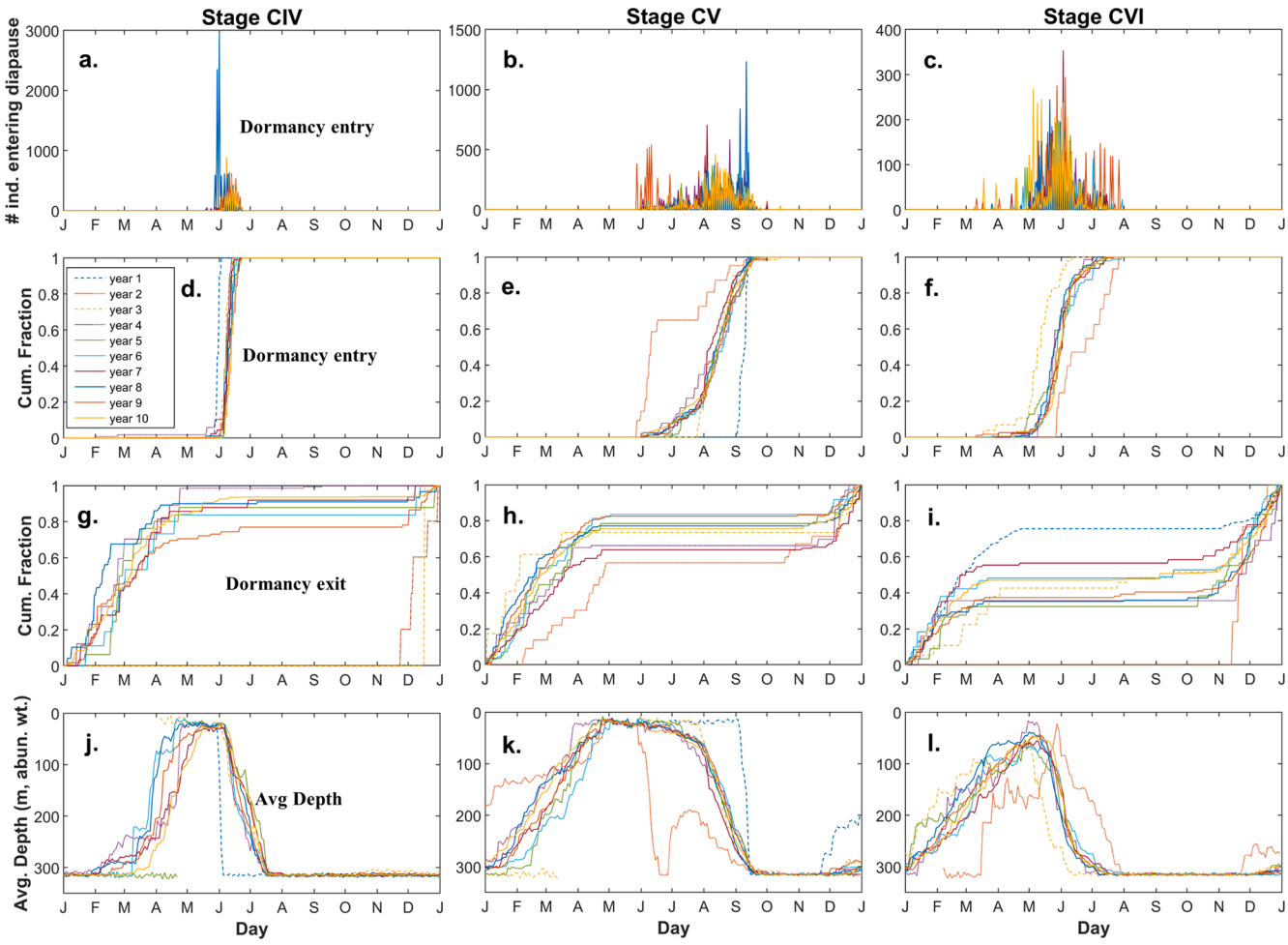

Fig. 8. Simulated dormancy entry and exit timing by year for (a.) CIV (left), (b.) CV (center), and (c) CVI (right). Dormancy exit for reproducing stages is reported as the day when gonad development or maturation begins, which for CV, also corresponds to the terminal molt to adult. For each stage, the plots include (a-c, top row) the frequency distribution of dormancy entry by year, (d-f, second row) the cumulative distribution fraction of entry day, (g-i, third row) the cumulative distribution fraction of exit day, and (j-l, bottom row) the abundance weighted average depth. Note top row vertical scale varies.

Table 2), we assessed assumptions about ingestion, assimilation, and respiration, and the effects of the net growth fraction that is routed to lipid. Adult size is a key property, from individual fitness to population dynamics, that is influenced by temperature, length of the feeding season and mortality risk. The model changes we implemented to reach the target sizes of late stages confirm that size plays a critical role in controlling life history transitions. In initial simulations, CIV and female individuals were small bodied with high lipid fractions (small and fatty), allowing females to accumulate significant lipid and even enter dormancy ahead of the spring bloom. Modifying the model was necessary to allow CIV to accumulate sufficient lipid to support diapause over ~8 months (July-March) and to acquire a larger body. They had to concurrently limit their growth during the low food conditions preceding the phytoplankton spring bloom while growing large quickly as soon as food was available in high concentrations. Hence, we enhanced their potential growth through a combination of increased food assimilation, decreased respiration, and an exploration of the lipid vs mass tradeoffs in the allocation of net growth. In contrast to typical copepod assimilation efficiency of 0.6 – 0.7, we relied on the higher range of 0.842 – 0.877 determined in *C. hyperboreus* feeding experiments by Tande and Slagstad (1985). As a result, food uptake was 44% higher and feeding stages grew faster when food concentration was not limiting.

Reducing basal respiration by 10% also improved the simulated late-stage size distributions and growth trajectories. Typical formulations for respiration assume a dependency on total body size (lipid plus structure), but this has been questioned repeatedly for large zooplankton with lipid sacs (Corkett & McLaren 1979, Visser et al. 2017) whose material (lipid reserves) is metabolically inactive. No clear relationships were determined between *C. hyperboreus* female respiration rates and temperature, dry weight, or carbon and nitrogen in Takahashi et al. (2002), while the food concentration produced the sole significant effect. In a *meta*-analysis of published respiration rates for fourteen copepod species, *C. hyperboreus* had the lowest temperature response (Maps et al. 2014a). In our model, the slower growth trajectory of CVs and the absence of the largest females may indicate that *C. hyperboreus* is assimilating too little or respiring too much, both being non-mutually exclusive. We found that the CIV individuals could not remain dormant from July until March unless the respiration rate in dormancy was further reduced by 25%. A full assessment of respiration in relation to food, late-stage structural mass, and lipid mass is outside the scope of the current study, but such an analysis could improve the mathematical formulation of *C. hyperboreus* respiration. Reducing respiration during periods of low food concentrations could move the model close to the female size target.

To simulate high lipid accumulation for late stages during the spring bloom while preventing significant growth before the bloom onset, we modified the model functional response. Decreasing ingestion at low food concentrations while increasing it slightly at high food concentrations allowed the model output to compare better to observed growth patterns. Despite this modification, simulated females did not grow to

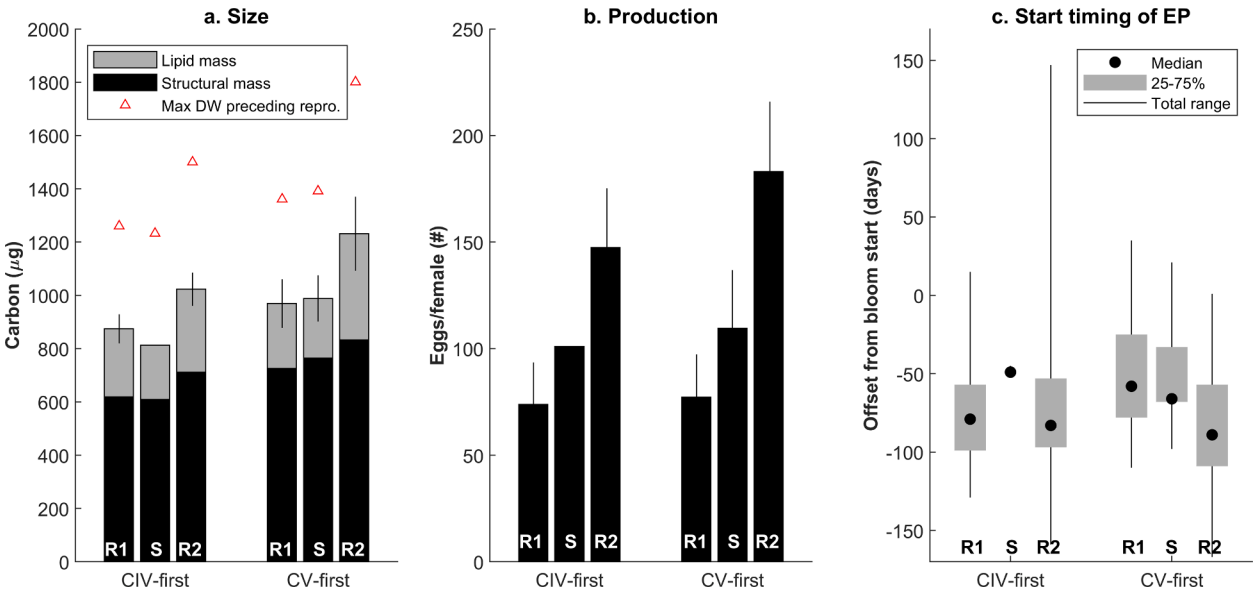

Fig. 9. Comparison of simulated life history characteristics of individuals from the CIV-first and CV-first dormancy phenotypes. Size, production, and timing characteristics are based on the cohort developing during the 7th model year at their first reproduction (R1 and S for iteroparous and semelparous females, respectively) and second reproduction (R2 for iteroparous females). Characteristics include (a) the abundance weighted mean size at the start of reproduction (μg carbon), shown as the sum of structural mass (black) and lipid mass (gray). The maximum dry weight preceding reproduction (red triangles) occurs at the start of dormancy, and is included to inform the size differences between the start of dormancy and the start of reproduction. Additional characteristics are (b) the mean total egg production (# eggs/female per reproductive event), and (c) the abundance-weighted timing of the start of egg production relative to the spring bloom onset, with negative and positive values respectively indicating the # days before and after April 9th, such that an offset of −100 days corresponds to January 1st. The thin black lines in a and b show +/- 1 standard deviation around the mean, except for the CIV-first semelparous phenotype since n = 2. Results for R1 and R2 are from the baseline simulation with second reproduction females (CIV-first: n = 34 particles, CV-first: n = 77 particles), and results for S are from the simulation without second reproduction females (CIV-first: n = 2 particles, CV-first: n = 29 particles). P-values from two-sample t-tests comparing differences in the means at the 5% significance level are reported in Table A4.

the upper end of the observed DW distribution. A recent study found that the ingestion rates of large copepods (*Neocalanus*) were greatly underestimated during grazing experiments due to improper experimental design based on usage of low volume incubation bottles (Takahashi et al. 2023). This may also be true for similarly large copepods such as *C. hyperboreus*. Additionally, model ingestion may be limited by the assumption of late stages performing diel vertical migration with a 50% daily probability, especially at the start of the spring bloom when hunger is potentially very high. In fact, observed late-stage vertical distributions from the Laurentian Channel in May (post-bloom) reveal *C. hyperboreus* were found within the upper 100 m with no day/night mode. While suggesting the absence of synchronous DVM, the vertical distribution could be explained by individuals feeding in the near surface chlorophyll maximum, and then sinking during digestion of each meal (S. Plourde, pers. comm., unpublished).

Lipid allocation during growth is a key parameter to correctly represent an individual's life cycle. With a high fraction of net growth routed to lipid, CIV individuals become fatty but remain small. Small-bodied CIVs developed into small-bodied CV and CVI, which were limited by their low structural mass and therefore lower ingestion in how much additional lipid they could accumulate. In contrast, a low fraction of net growth routed to lipid produced individuals that could ingest more and grow faster, since ingestion increases faster than respiration. This resulted in a lower lipid fraction for large-bodied and lean CIVs. Such CIVs were challenged to exceed the lipid threshold for diapause entry, but eventually developed into much larger females which could pack on high quantities of lipid after their structural growth ceased. Based on observations that structural mass is generally developed first across the animal kingdom (e.g., Butterfield et al. 1983), we considered allocating a variable rate of net growth to lipid, dependent on molt cycle fraction. In a model with a sophisticated description of *C. finmarchicus* metabolism (Anderson et al. 2022), food macronutrients were allocated differently to build body structure and lipid, such that food-derived lipid was prioritized for building lipid stores, while absorbed protein and carbohydrate were used to build the body structure up to a maximum size, after which the individual preparing to enter diapause synthesized lipid from protein and carbohydrates. Ultimately we decided against the approach since within-stage cyclicity in the lipid accumulation may lead to spurious outcomes in a model with behaviors dependent on lipid ratios. In addition, detailed knowledge of the copepods' prey quality is required. We concluded that a simpler, constant allocation rate would avoid non-linear responses, and selected a value balancing the body structure and lipid accumulation (65%). Once the constant lipid accumulation rate was implemented, we also allowed stage CIII – which does not overwinter in the GSL – to accumulate a small lipid content (max 10% DW as lipid). With this change for CIII, CV individuals were 30% larger in structural mass with equivalent lipid mass, and 20% larger by carbon dry weight, highlighting the complex trade-offs in building body structure vs lipid mass.

A mechanistic link between lipid fullness and dormancy transitions in the model produces CIV and CVI phenology close to observations, but further adjustment may improve the probability of CIV entry into dormancy and the timing of CV entry. The model simulates the seasonal patterns of increases in population-mean lipid with the spring bloom onset, peaking at mid-summer when dormancy entry occurs, followed by a slow decrease in lipid until the end of dormancy and reproduction in the winter. We expected the model to be highly sensitive to the lipid threshold used for life-cycle transitions, but the implementation of individual variability in both growth trajectories and the dormancy entry and exit parameters buffers the impact of that choice in a realistic way.

Nonetheless, for most CIV individuals, the lipid threshold was not achieved before development to the next stage (CV). Many of that G0 cohort developing to CV continued slowly growing and accumulating lipid in the surface and entered dormancy 1–2 months later than observed. These model results indicate that using lipid thresholds as the sole trigger to enter dormancy may be insufficient. Observations of the

Arctic congener *C. glacialis* leaving the surface layer once it warms beyond a certain temperature (Kosobokova 1999, Niehoff & Hirche 2005) point to the potential for a thermal trigger for *C. hyperboreus*. In the northwest Atlantic, temperatures >5 ℃ and >5.5 ℃ in the top 50 m had a strong negative association with late-stage abundance of *C. glacialis* and *C. hyperboreus*, respectively (Albouy-Boyer et al. 2016), while CPR surface sampling on the south Newfoundland shelf showed both species left the near surface with similar timing (Head & Pepin 2010). In the model forcing, temperatures exceed 5.5 ℃ in the top 6 m in early July, corresponding to the observed peak entry into diapause in the GSL (Fig. 3). Additionally, reducing the temperature coefficient of respiration (p), may be reasonable for *C. hyperboreus*, to allow greater active growth and lipid accumulation in stage CIV, since it has the lowest activation energy (slope of metabolic rate in relation to temperature) of the fourteen copepod species assessed in Maps et al. (2014a). Conover (1962) had found no significant increase in respiration with temperature ($Q_{10} = 1.14$) for acclimated CV. Since late stages encounter warming conditions in the upper layer between the spring bloom in April and the observed diapause entry in late June to early July, reducing the respiration temperature response could increase the probability of dormancy entry by enabling faster lipid buildup.

6.3. Relative success of different phenotypes

The baseline model simulated a population structure and phenology similar to the literature targets, except for the late diapause entry by most CV. Contrasting the baseline simulation with the model experiment performed without second reproduction females reveals a key role for the multiyear life cycle in bolstering the resilience of the population. The baseline population with second reproduction females grew from its minimum in Year 2 to more than double by Year 10, whereas the experiment without second reproduction females decreased by about one-third from Year 2 to Year 10. Simulated second reproduction females increase their structural mass by an additional 15% and subsequently convert all net growth into stored lipid, resulting in greater maximum dry weight, higher lipid content, and higher fecundity. By including the second reproduction female strategy in the model, the new generation developing in Year 7 has almost twice the cumulative lifetime production. Also, the wider time window of egg production under iteroparity increases the probability that some offspring will survive to reproduce, thereby contributing to population stability via a bet-hedging strategy. Iteroparity should be considered in the context of a suite of evolutionary responses to strong seasonality in a stochastic environment (Varpe 2017, Varpe & Ejsmond 2018a). Seasonality requires life history tradeoffs to be made by an organism, such as balancing growth and reproduction, or future survival against current reproduction (Stearns 1989). While incurring the costs of not maximizing reproduction as a first year female and higher mortality risk due to the lengthened life cycle, *C. hyperboreus* transfers energy to the next year by reserving some portion of its lipid to invest in future reproduction. Evolutionary theory also suggests that iteroparity generally reflects lower mortality in adults than in young stages (Varpe & Ejsmond 2018a), which supports our model mortality formulation of decreasing risk with increasing stage. Here, the model experiments suggest that the second-reproduction female strategy contributes to both increased production and population stability. Although a specified strategy in our model, iteroparity in the GSL and other sub-Arctic environments emerges as an approach to achieve high fecundity under the uncertainty of a good vs bad year for acquiring resources and recruitment (Varpe 2017).

The CIV-first dormancy phenotype may also contribute to the stability of the population. Since CIV enter dormancy earlier in the model, survival to the point of dormancy entry is higher for CIV, while their survival to reproduction is lower owing to an additional growth season as CV. The CIV-first dormancy phenotype may increase the phenological range with variable timing of dormancy exit and CV lipid accumulation, leading to larger variability in population dynamics timing. This variability buffers the population from the effects of a single poor year and gives that cohort the opportunity to reproduce 1–2 years after the bad year. In contrast, a cohort developing to CV during a bad year likely enters dormancy small, developing to adult without a lipid reserve sufficient to support high R1 egg production. Although those small females accumulate additional lipid before the second dormancy period, their lipid storage capacity would be limited by smaller body size, which translates into fewer eggs produced during R2.

In the baseline simulation, most individuals entering dormancy as stage CIV are spawned earlier in the year, as this timing allows a rapid growth and lipid accumulation early on. Individuals spawned later have a mismatch with the spring bloom and do not exceed the CIV lipid fraction threshold for entering dormancy, thus developing into CV that will accumulate lipids slower in the warm and low food conditions of the post-bloom environment. These individuals will produce the CV-first dormancy phenotype that finds a counterintuitive success in the model, as it grows slowly in the surface layer into larger individuals eventually entering dormancy in late summer. This CV late entry into dormancy remains a blind spot of the model, since it has been observed that the arctic *C. glacialis* may leave the surface layer once it warms beyond a certain temperature (Niehoff & Hirche 2005), as described above. If *C. hyperboreus* were to have a similar response to surface warming, then CV individuals could potentially enter dormancy by July, improving the simulated dormancy phenology. Despite our efforts to implement a coherent mechanism of dormancy entry for CIV-CV stages, the lack of information on this process remains a source of uncertainty for any model.

It is interesting that our model allowed the successful coexistence of the two dormancy phenotypes to emerge and persist throughout the 10-year baseline simulation. This indicates that both phenotypes must be similar in fitness. The CIV-first dormancy phenotype has slightly higher survival the first year, but it does not achieve the higher maximum female dry weights of the CV-first dormancy phenotype. The simulated differences in female size and lipid seem to be related to the CV size and timing from the model, which could be considered satisfactory for the CIV-first phenotype, but less so for the CV-first phenotype. On one hand, CIVs entering dormancy develop into G1 CVs the following spring, growing to a moderate size and reproducing the observed dormancy entry timing in early July. On the other hand, while the CV-first dormancy phenotype is able to edge out the CIV-first phenotype in abundance and in terms of total egg production, the weak comparison to observed patterns and the unrealistic shift of the growth period late into July-August show it may not be a realistic strategy in the GSL. However, we note that the CV-first dormancy strategy was abundance-dominant over the CIV-first dormancy strategy in eastern Fram Strait based on sediment trap sampling (Tokuhiro et al. 2024). More observations are needed to sort out the relative fitness of both strategies. Sorting out the relative fitness of both strategies is likely to involve a closer comparison of the semelparous and iteroparous females' phenotypes. The timing of reproduction contracts and starts later under semelparity. This narrower, later window for egg production results in fewer eggs that develop to match the spring bloom as stage CIV, and the model population is then dominated by the CV-first diapause phenotype. This provides evidence of a strong link between the occurrence of second reproduction females and the fitness of the CIV phenotype. Moreover, when second reproduction females are not present, the simulated abundance declined relative to the population with second reproduction females, pointing to lower population success without iteroparity in the GSL.

6.4. Limitations and caveats

An axiom of numerical modelling, attributed to the statistician George Box (1976), states that while all models are wrong, some models are useful. We have shown that the model developed for the *C. hyperboreus* population in the GSL has utility, however several model

limitations related to the 1-D model setup, visual predation, and assumptions for overwintering life stages hold the potential to affect model results. Configuring the model in 1-D ignores lateral advection of copepods, while allowing us to test the species description in a quasi-realistic environment that includes the effects from horizontal advection on ocean temperature, food, and light, since GSBM is a 3-D biophysical regional ocean model (Lavoie et al. 2021). Active *C. hyperboreus* nauplii and copepodites may be transported horizontally in the near surface during their active period, potentially entering the Anticosti Gyre via the westward-flowing North Shore Current to the north or the eastward-flowing Gaspé Current to the south. We expect such error to be minimized within the Anticosti Gyre, where horizontal transport is generally low relative to the coastal currents to the north and south, and residence time is higher than the surrounding upper layer waters. Dormant late stage *C. hyperboreus* reside at depth in the Atlantic water layer of the Laurentian Channel, where they are subject to a low velocity westward displacement associated with the estuarine deep water return flow (Plourde et al. 2003, Maps et al. 2014b, Lavoie et al. 2016).

While we implemented a simple visual predation mortality in the model, interactions between ambient light, body size, vertical position, and visual predation have been theorized and described for different marine environments (Miller et al. 1991, Aksnes & Giske 1993, Dupont & Aksnes 2012, Ohman & Romagnan 2016). Neglecting body size in the simulated visual predation mortality could lead to underestimating mortality for the largest copepods where there is sufficient ambient light for visual detection. While the model's smoothed euphotic zone partially compensates for the underestimate, since it extends deeper than observed, it would increase the effect of visual predation mortality across all naupliar and copepodite body sizes. Increased visual detection of larger copepodites in the euphotic zone could impact the relative success of different dormancy phenotypes in the model. For example, if survival of the largest females were to decline, then we would expect fewer eggs produced by second reproduction females. Also, higher relative visual predation on the larger CV-first vs smaller CIV-first dormancy phenotype could increase the relative fitness of the CIV-first phenotype. However, how visual and non-visual predation effects may interact in the sea ice- and CDOM-shaded GSL water column to impact the *C. hyperboreus* population is unconstrained by observations.

If stage CIII individuals were able to successfully overwinter in the GSL, then this would be missed in our model which assumes CIV is the first stage capable of entering dormancy. Overwintering CIIIs could lengthen the *C. hyperboreus* life cycle and would likely increase the population resilience in the GSL. Generally, stage CIII contributes very little to the overwintering stage structure across the northwest Atlantic, based on AZMP stage abundances sampled during October-December in years 1999–2012. Trace CIII abundance (~2.5%) is observed in the GSL in the fall (S. Plourde, Pers. Comm. 2024), similar to the overwintering stage structure with low CIII contributions observed in other sub-Arctic environments such as Iceland (Astthorsson & Gislason 2003, Gislason 2018) and in the Barents Sea (Melle & Skjoldal 1998), and in contrast to the Arctic Ocean (Dawson 1978). Therefore, our model is representative of *C. hyperboreus* throughout sub-Arctic environments. Due to the trace abundance of CIII in the overwintering population in the GSL, we consider the potential error associated with our assumptions about overwintering stages to be small.

7. Conclusions

Our *C. hyperboreus* population model for the GSL combines together, for the first time, the representation of free-evolving individual lipid content and a mechanistic description of ontogenetic dormancy and vertical migration strategies in response to this individual lipid content. To respect our current knowledge of the species' life cycle, the model had to simulate a handful of key biological processes, while allowing interindividual variability: ingestion and metabolism related processes, allocation to lipid stores, emerging (flexible) diapause strategies and the possibility for females to reproduce a second year after dormancy. The model results showed that without second reproduction females, few CIVs entered diapause due to a mismatch with the spring bloom, and the simulated population contracted. Coexistence of multiple, persistent phenotypes resulted from the model's ability to balance energy allocations under variable environmental conditions, leading to various individual emerging life-cycle strategies and trajectories. This model may therefore be well suited to examine hypotheses about how *C. hyperboreus* individuals and populations respond under rapidly changing environmental conditions.

During model development, we were able to identify key knowledge gaps that would benefit from additional measurements: *C. hyperboreus* late stage size distribution (with a focus on interindividual variability) made in conjunction with estimates of lipid content (*e.g.*, lipid sac area and volume from digital image analysis, chromatographic lipid mass analysis, *etc.*), as well as continued support for observations of reproduction timing and egg production in the GSL. Targeted observations in conjunction with model-based inquiry can help inform how life-history tradeoffs may change in the GSL under future warming and whether *C. hyperboreus* can find success due to its high plasticity.

CRediT authorship contribution statement

Catherine E. Brennan: Writing – review & editing, Writing – original draft, Visualization, Validation, Methodology, Investigation, Conceptualization. **Frédéric Maps:** Writing – review & editing, Supervision, Methodology, Investigation, Conceptualization. **Diane Lavoie:** Writing – review & editing, Data curation. **Stéphane Plourde:** Writing – review & editing, Supervision, Project administration, Methodology, Investigation, Data curation, Conceptualization. **Catherine L. Johnson:** Writing – review & editing, Supervision, Resources, Project administration, Methodology, Investigation, Funding acquisition, Conceptualization.

Declaration of competing interest

The authors declare that they have no known competing financial interests or personal relationships that could have appeared to influence the work reported in this paper.

Data availability

Data will be made available on request.

Acknowledgements

Funding from Fisheries and Oceans Canada's Whales Initiative has supported this work, as part of an investment in scientific research to improve understanding of North Atlantic right whale prey availability and foraging habitat. This work is a contribution to the research program of the strategic cluster of oceanography research Québec Océan, the International Research Laboratory Takuvik (3376) from CNRS and the Sentinelle Nord strategy from Université Laval. We thank John Newgard for his graphic design work on Fig. 1, Caroline Lehoux for the AZMP zooplankton data analysis shown in Fig. 2, the NASA OBPG for the ocean color satellite data (https://oceancolor.gsfc.nasa.gov/), and the BIO remote sensing group for the PhytoFit application. The manuscript was improved by the comments of Wendy Gentleman, Kira Krumhansl, and Kevin Sorochan, and we thank the two anonymous reviewers for their constructive feedback. Also, we are grateful for the Fortran code modifications by Shihan Li and Kyoko Ohashi. Shihan Li coded the biological equations and a repeat-year forcing option, and devised the scheme for storing a large number of empty particles at the domain edge. Kyoko Ohashi contributed code for writing restart files and running the model from a hot start, and recycling dead particles, to be incorporated in future modelling experiments.

Appendix A. *C. hyperboreus* model details

Table A1
List of model state variables and parameters. Values are taken from Bandara et al. (2019; 'B19') and based on Maps et al. (2012b). When values in this study differ from those of the previous study (B19), we list the original value in B19 in parentheses. Note that parameters that were evolvable (soft) in B19 but converged consistently to one value are fixed in this study ("rate" of net growth routed to lipid). L and M denote lipid carbon mass and structural carbon mass, respectively.

State Variable/Parameter	Value (B19 orig.)	Unit	Note
State Variables			
Particle ID		integer	
Maternal ID		integer	
Position (X, Y, Z)		decimal degrees (X, Y), m (Z)	
Age		days	
Stage		real number	0.0 (egg) – 12.0 (adult)
Activity		integer	0 = active, 1 = dormant, 2 = gonad mat/devel, 3 = egg prod
Sex		integer	0 = non-adult, 1 = male, 2 = $CVIF_{R1}$, 3 = $CVIF_{R2}$
Structural Mass (*mass*)		µg C ind^{-1}	
Lipid Mass (*lipid*)		µg C ind^{-1}	tracked for stage ≥ CIII
Daily # eggs produced		# $female^{-1}$ d^{-1}	
Cumulative # eggs produced		# $female^{-1}$	
Start of egg production		date number	for $CVIF_{R1}$ & $CVIF_{R2}$
Spawning duration		days	for $CVIF_{R1}$ & $CVIF_{R2}$
Max structural mass achieved (*mass_max*)		µg C ind^{-1}	starvation metric, to apply starvation mortality
Max female mass (*mass_limit*)		µg C ind^{-1}	growth metric, 115% of mass at terminal molt
Initial lipid mass		µg C ind^{-1}	dormancy metric, for tracking lipid utilization
Lipid floor		%	egg prod metric, 0% $CVIF_S$ & $CVIF_{R2}$, 15% $CVIF_{R1}$
Parameters			
Fixed (hard) parameters			
a, food assimilation coefficient	0.86375 (0.6)		Mean in Tande and Slagstad (1985)
b, mass coefficient of ingestion	0.01319		
m, mass exponent of ingestion	0.7516		
c, temperature coefficient of ingestion	1.1833		
n, temperature exponent of ingestion	0.0761		
f, mass coefficient of metabolism	0.0010377 (0.001153)		Reduced −10%
	0.00077828		Dormant CIV: further reduced −25%
o, mass exponent of metabolism	0.7502		
g, temperature coefficient of metabolism	1.2065		
p, temperature exponent of metabolism	0.0849		
we, weight of egg	0.83	µg C	
a_dev, stage-specific development coefficient	1495		Egg
	974		NI
	1461		NII
	3485		NIII
	1907		NIV
	1799		NV
	2113		NVI
	2427		CI
	2856		CII
	3588		CIII
	5433		CIV
	10,259		CV
	0		CVI
molt_crit	2.86	µg C	NIV
	5.63	µg C	NV
	9.70	µg C	NVI
	16.95	µg C	CI
	39.55	µg C	CII
	88.99	µg C	CIII
	204.15	µg C	CIV
	554.96	µg C	CV
m1, first term of mortality equation	0.6 (2.0*)	day^{-1}	
m2, second term of mortality equation	0.7 (~0.4 – 0.75*)		
Tref, reference temperature for mortality	7.5 (~4.5–10*)	°C	
k_d, water column light attenuation coefficient	0.06	m^{-1}	
k_f, half saturation of ingestion	27.0	µg C $liter^{-1}$	
k_{ff}, half saturation of development (low food)	10.0	µg C $liter^{-1}$	
rate, energy allocation to lipid	0.65 (0.70)		
terminal molt sex ratio	80	% female	
z_{opt}, optimal depth	25	m	Egg-NII
	z(0–75) of max potential growth	m	NIII-CVI

(*continued on next page*)

Table A1 (*continued*)

State Variable/Parameter	Value (B19 orig.)	Unit	Note
	z, mid-bottom grid cell	m	Dormant, reproducing
	100	m	If DVM, dawn-dusk
DVM, diel vertical migration	0.5	probability day^{-1}	Active CIV-CVI
sigma, vertical spread coefficient, ~volatility	0.15	$second^{-0.5}$	
theta, vertical "swimming" speed coefficient	0.0001	$second^{-1}$	
dt, time step of model	1800	second	= 30 min time step
Variable (soft) parameters			
d_{in}, lipid fraction threshold for diapause entry	CIV: 0.33–0.40 (0.41) † CV-CVI: 0.41–0.47 (0.41) †	unitless: L/(M+L)	
d_{out}, lipid fraction used since diapause entry, threshold for diapause exit	CIV: 0.75–0.95 (0.29) † CV-CVI: 0.45–0.65 (0.29) †	unitless: L/(M+L)	

*Reference value for *C. finmarchicus* at Anticosti Gyre from Maps et al. (2012a). †Lipid fraction values in parentheses correspond to the mean optimal parameter value in the L baseline simulation of Bandara et al. (2019).

Table A2
Biological model equations describing *C. hyperboreus* individual biology and behavior, as in Table 2 with additional definitions (third column), references (fourth column), and key differences in this study vs previous studies (fourth column where relevant). Equations represent stage development and molting, respiration, ingestion and assimilation, growth and lipid accumulation, reproduction including gonad maturation and development and egg production, starvation, mortality, dormancy entry and exit thresholds, and vertical displacement.

Category	Equation	Definitions	References
Development	$D = a\_dev \cdot (T + 13.66)^{-2.05} \cdot f\_lim$ where $f\_lim = F^2/(k_{ff}^2 + F^2)$ $MCF(t) = MCF(t-1) + dt/D$	*a_dev* = stage-specific development coefficients; F=food concentration (μg C L^{-1}); MCF=molt cycle fraction (0–1), indicating development within stage.	Bělehrádek 1935, Ji et al. 2012, this study for Type III food limitation term.
Molting	Occurs if stage development suggests $MCF \geq 1$ & if $mass \geq molt\_crit$	Stage-specific values for *molt_crit* = W_J^{max}, listed for the "M−Environment" of B19 in their table B1. Development is paused while *mass* < *molt_crit*.	Bandara et al. (2019)
Growth	$G = a \cdot I - R - EP$	*G*=growth rate (μg C ind^{-1} $timestep^{-1}$) with timestep dt = 30 min. *I*=ingestion, is modified by *a*, the food assimilation coefficient. *R*=respiration, *EP*=egg production. Unassimilated food (*i.e.*, egestion = (1-a)·I) is untracked.	Bandara et al. (2019); this study increased food assimilation, *a*.
Starvation	If $G<0$: If $lipid(t) \geq |G|$, then $lipid(t+1) = lipid(t) + G$, If $lipid(t) < |G|$ or $lipid = 0$, then $mass(t+1) = mass(t) + G$	Once lipid stores are depleted, structural mass may be drawn down by as much as 10%, with mortality increasing linearly with mass depletion until M=1 at 10% depletion.	Bandara et al. (2019)
Lipid accumulation	If $G>0$ and *stage* ≥ CIII: If *mass* < 38 μg C ind^{-1}, then *lipid* = 0. If *mass* falls between 38–159 μg C ind^{-1}, then lipid allocation rate increases exponentially from 0 to 0.65. If *mass* > 159 μg C ind^{-1}, then $lipid(t+1) = lipid(t) + rate \cdot G$, where rate = 0.65. Exceptions: CIII *lipid* capped at 10% DW as lipid; CIV-CVI capped at 70% DW as lipid. Females after terminal molt: can increase structural mass by 15%, after which CVIF cease structural growth and allocate net growth entirely to lipid: $lipid(t+1) = lipid(t) + G$.	Following the terminal molt to adult, females can further increase structural mass by 15% to represent the terminal molt. The cap of 70% DW as lipid was implemented to avoid unrealistically large females, but this condition is never met in the model. By comparison, Bandara et al. (2019) utilized a cap of 41% DW as lipid, which was always met in their model for *C. hyperboreus*.	Bandara et al. (2019); this study for treatment of CIII-CVI lipid fraction caps and CVIF additional mass growth of 15%.
Ingestion	$I_{REF} = 0.5 \cdot b \cdot M^m$ $I = I_{REF} \cdot c \cdot exp(n \cdot T) \cdot \frac{F^2}{k_f^2 + F^2}$	I_{ref} is ingestion (μg C ind^{-1} $timestep^{-1}$) at reference temperature of -2C, here multiplied by 0.5 to account for the model timestep (dt = 30 min). M is *mass*, T is ambient temperature (℃). Ingestion coefficients (b, m, c, n) are listed in Table S1.	Bandara et al. (2019); this study replaced their scaling term with a Type III food limitation term to limit growth at low food.
Respiration	$R_{b\_ref} = 0.5 \cdot f \cdot (M + L)^o$ $R_b = R_{b\_ref} \cdot g \cdot \exp(p \cdot T)$ $R_a = 1.5 \cdot R_b$ $R_{active} = R_b + R_a$ $R_{dormant} = 0.25 \cdot R_b$ $R_{repro} = 0.62 \cdot R_b$	R_{b_ref} is basal respiration (μg C ind^{-1} $timestep^{-1}$) at a reference temperature (−2 ℃), which is multiplied by 0.5 to account for the model timestep (dt = 30 min). *M* is *mass*, *L* is *lipid*. Basal respiration, R_b, also depends on ambient temperature *T* (℃). Coefficients of respiration (*f*, *o*, *g*, *p*) are listed in	Bandara et al. (2019); this study introduced R_{repro} and decreased parameter *f* and CIV $R_{dormant}$.

(*continued on next page*)

Table A2 (*continued*)

Category	Equation	Definitions	References
		Table S1. Active individual total respiration is the sum of basal (R_b) and active (R_a) respiration. While dormant or reproducing, $R_a = 0$, and R_b is reduced (details in text).	
Gonad development & maturation	3 week delay before spawning		This study
Egg production	$EP = 2 \cdot R_b$ $lipid = lipid - EP$ If $lipid \leq lipid\_floor$, then EP ends For $CVIF_{R1}$: $lipid\_floor = 0.15 \cdot max\_diap\_lipid$ For $CVIF_{R2}$ & $CVIF_S$: $lipid\_floor = 0$	*EP*, egg production (μg C ind^{-1} $timestep^{-1}$), is proportional to the individual basal respiration, and egg matter is converted from *lipid*. EP occurs until the *lipid_floor* is reached, 0 for semelparous females and $CVIF_{R2}$, and 15% of the maximum lipid at the start of diapause for $CVIF_{R1}$. Conversion to egg numbers uses an egg C content of 0.83 μg. Eggs are released in clutches of 75 eggs.	This study scales EP with R based on data from Plourde et al. (2003), which differs from EP=G in Bandara et al. (2019) and Maps, Pershing, Record (2012). Egg C weight follows Plourde et al. (2003).
Dormancy entry	$lipid\_frac = lipid/(lipid + mass)$ If $stage \geq first\_diap\_stage$ & $lipid\_frac \geq d_{in}$ & $activity = 0$, then $flag\_enter\_diap$ = T For CIV-CV: If $flag\_enter\_diap$ = T, & MCF ≥ 0.98 & $activity = 0$ (active), then activity = 1 (dormant) For CVIF: If $flag\_enter\_diap$ = T & $activity = 0$ (active), then $counter\_c6\_active = counter\_c6\_active + dt$ If $counter\_c6\_active \geq$ 3 weeks & $activity = 0$ (active), then $activity = 1$ (dormant) For all stages at entry into dormancy: $max\_diap\_lipid = lipid$	The lipid fraction, *lipid_frac*, represents the proportion of DW as lipid. The first stage capable of entering dormancy (*first_diap_stage*) is specified in the model input file. The lipid threshold for following the dormancy entry pathway, d_{in}, is sampled for each particle from a uniform distribution in the range [0.33–0.41] for stage CIV, and that value is transformed to the higher range [0.41–0.47] for stages CV-CVI. *MCF*=molt cycle fraction, is the fractional distance through the current developmental stage. If the conditions are met to enter dormancy based on stage, lipid fraction, and activity, then *flag_enter_diap* is set to *true*. Once on the dormancy pathway, individuals continue foraging in the surface active layer and enter dormancy once they have ~ completed their current stage development (*MCF*≥0.98 for CIV-CV), or in the case of CVIF for whom *MCF* is undefined, they remain active for 3 weeks, tracked by *counter_c6_active*. *max_diap_lipid,* the lipid amount at dormancy entry, is recorded.	This study specifies higher thresholds for individuals preparing to reproduce (CV-CVIF), and allows individuals to continue growing in surface active layer until end of stage (or 3 weeks for CVIF).
Dormancy exit	$lipid\_frac\_burned = (max\_diap\_lipid - lipid)/max\_diap\_lipid$ if $lipid\_frac\_burned \geq d_{out}$, then $flag\_exit\_diap$ = T If $flag\_exit\_diap$ = T, then: For CIV: $activity = 0$ (active), $stage = 11.0$ For CV: $sex = 1$ (females), $abund = 0.8 \cdot abund$ (kill males), $stage = 12.0$, $mass\_limit = mass \cdot 1.15$, $activity = 2$ (gonad development) For CVIF: $activity = 2$ (gonad maturation)	*lipid_frac_burned* tracks the proportion of the lipid reserve utilized since entering dormancy. d_{out} is the lipid utilization threshold for molting and exiting dormancy (CIV) or for performing the terminal molt to female and beginning reproduction (CV-CVI). It is sampled for each particle from a uniform distribution in the range [0.44–0.64] for CV-CVI, or [0.75–0.95] for stage CIV. Exit from dormancy follows a stage-dependent sequence: CIVs molt to CV and ascend. CVs molt to female, kill males, CVIF structural mass upper limit is specified (*mass_limit*), gonad development begins. CVIF begin gonad maturation.	Bandara et al. (2019); this study increased d_{out} for stage CIV since they are not preparing to reproduce, and implemented larger structural mass potential for second-reproduction females.
Vertical displacement	OU biased random walk: $z(t+1) = rand \cdot sd + z_{opt} + (z(t) - z_{opt}) \cdot \exp(-theta \cdot dt)$	OU is the Ornstein-Uhlenbeck equation for vertical displacement, here calculated each 30 min	Benkort et al. (2020). This study: depth of active layer after Plourde et al. (2003);

(*continued on next page*)

Table A2 (*continued*)

Category	Equation	Definitions	References
	Where *rand* = random number 0–1, and $sd = sigma \cdot sqrt\left(\frac{1-\exp(-2 \cdot theta \cdot dt)}{2 \quad theta}\right)$	timestep, following a biased random walk towards optimal depth z_{opt} with random error superimposed, resulting in a vertical spread around the target depth.	depth of dormant optimal depth after Krumhansl et al. (2018).
Mortality	M(total) = M(natural + predation) + M(starvation) + M(senescence) + M(death of males), where M(natural + predation) is: $m = I' \cdot (0.01 + m1 \cdot \exp(-m2 \cdot stage)) \cdot \left((Tref + 13.66)^{-2.05}\right) / \left((T + 13.66)^{-2.05}\right)$ Where light L at depth z: $L(z) = PAR_{surf} \cdot \exp(-k_d \cdot z)$ And, $I' = ((\max 2 - \min 2)/(\max 1 - \min 1)) \cdot (L(z) - \max 1) + \max 2$ Dormant & reproducing: $m = 0.1 \cdot m$ Active CIV-CVI in September-December: $m = 2.25 \cdot m$ $M(starvation) = \min(1, 2 \cdot mass_{burn})$ *if* $0.1 < mass_{burn} \leq 0.5$, where $mass_{burn} = (mass\_max - mass)/mass\_max$ M(death of males) = Males killed at terminal molt: Abun(t + 1) = 0.8·Abun(t)M (senescence) = Spent females die after egg production: Abun(t + 1) = 0	I' is a scaling term (1–1.5) that represents increased mortality due to visual predation based on the ambient light at depth, L(z). Due to uncertainty in vertical positioning, we set a lower k_d for the northwest GSL to influence visual predation mortality over the active layer under high light.	Bandara et al. (2019); this study I' depends on light but not body size.

Table A3
Emergent vs prescribed *C. hyperboreus* model properties. For each category in the left column, the emergent vs prescribed (*i.e.*, specified as input to the model) model properties are listed.

Category	Emergent	Prescribed
Size	◂ structural mass ◂ lipid mass ◂ dry weight ◂ lipid fraction	◂ minimum structural mass for each stage ◂ egg weight
Timing	◂ dormancy entry ◂ dormancy exit ◂ dormancy duration ◂ egg production start ◂ spawning duration	◂ time evolution of environment (spring bloom, temperature, and surface photosynthetically active radiation) via GSBM forcing ◂ duration of gonad development-maturation phase (3 weeks) ◂ duration of CVIF in surface active layer after triggering dormancy pathway (3 weeks)
Production	◂ daily eggs per female ◂ cumulative eggs per female ◂ total egg production	
Behavior	◂ CIV- or CV-first dormancy phenotypes	◂ first dormancy stage (CIV) ◂ iteroparous female strategy (on or off)

Table A4
Statistical summary of significant differences in the mean for size, production, and timing of reproduction among the CIV- and CV-first dormancy phenotypes shown in Fig. 9. P-values are reported comparing the sample mean between two categories using a two-sample *t*-test at the 5% significance level, with bold values indicating p-value <0.05. Very small non-zero values are reported as ≪0.001. Note that EP1 and EP2 represent their first and second reproduction respectively, with EP2 only occurring for iteroparous females.

	Semelparous		Iteroparous			
	First Reproduction (EP1)		**First Reproduction (EP1)**		**Second Reproduction (EP2)**	
	CIV_S_EP1	**CV_S_EP1**	**CIV_I_EP1**	**CV_I_EP1**	**CIV_I_EP2**	**CV_I_EP2**
Mass						
CIV_S_EP1	NA					
CV_S_EP1	**≪0.001**	NA				
CIV_I_EP1	**≪0.001**	**≪0.001**	NA			
CV_I_EP1	**≪0.001**	**≪0.001**	**≪0.001**	NA		
CIV_I_EP2	**≪0.001**	**≪0.001**	**≪0.001**	**≪0.001**	NA	
CV_I_EP2	**≪0.001**	**≪0.001**	**≪0.001**	**≪0.001**	**≪0.001**	NA
Lipid						
CIV_S_EP1	NA					
CV_S_EP1	**≪0.001**	NA				
CIV_I_EP1	**≪0.001**	**≪0.001**	NA			
CV_I_EP1	**≪0.001**	**≪0.001**	**≪0.001**	NA		
CIV_I_EP2	**≪0.001**	**≪0.001**	**≪0.001**	**≪0.001**	NA	
CV_I_EP2	**≪0.001**	**≪0.001**	**≪0.001**	**≪0.001**	**≪0.001**	NA

(*continued on next page*)

Table A4 (*continued*)

	Semelparous		Iteroparous			
	First Reproduction (EP1)		**First Reproduction (EP1)**		**Second Reproduction (EP2)**	
	CIV_S_EP1	**CV_S_EP1**	**CIV_I_EP1**	**CV_I_EP1**	**CIV_I_EP2**	**CV_I_EP2**
DW						
CIV_S_EP1	NA					
CV_S_EP1	**≪0.001**	NA				
CIV_I_EP1	**≪0.001**	**≪0.001**	NA			
CV_I_EP1	**≪0.001**	**≪0.001**	**≪0.001**	NA		
CIV_I_EP2	**≪0.001**	**≪0.001**	**≪0.001**	**≪0.001**	NA	
CV_I_EP2	**≪0.001**	**≪0.001**	**≪0.001**	**≪0.001**	**≪0.001**	NA
Production						
CIV_S_EP1	NA					
CV_S_EP1	**≪0.001**	NA				
CIV_I_EP1	**≪0.001**	**≪0.001**	NA			
CV_I_EP1	**≪0.001**	**≪0.001**	0.1428	NA		
CIV_I_EP2	**≪0.001**	**≪0.001**	**≪0.001**	**≪0.001**	NA	
CV_I_EP2	**≪0.001**	**≪0.001**	**≪0.001**	**≪0.001**	**≪0.001**	NA
Timing						
CIV_S_EP1	NA					
CV_S_EP1	0.712	NA				
CIV_I_EP1	**≪0.001**	0.9077	NA			
CV_I_EP1	0.8026	0.7473	**≪0.001**	NA	0.9982	
CIV_I_EP2	0.9224	0.9077	**≪0.001**	0.9982	NA	
CV_I_EP2	**≪0.001**	**≪0.001**	**0.0101**	**≪0.001**	**≪0.001**	NA

Description of biological equations

A.1. Vertical target depth

C. hyperboreus optimal depths are specified based on stage and activity state, and can vary with *in situ* temperature and food conditions for active stages, or with bottom depth for dormant or reproducing individuals. Due to the biased, random walk formulation for vertical movement (Ornstein-Uhlenbeck equation), individual particles generally move towards the optimal depth, but due to the random noise component there is a spread around the optimal depth (S.D. ~6 m), and particles are displaced vertically at each model 30-minute time step. The optimal depth of early non-feeding stages (egg-NII) is set at 25 m. Active feeding stages (NIII-CVI) seek out the depth in the upper 75 m that maximizes potential growth based on *in situ* temperature and food conditions. Particles representing late stages (CIV-CVI) have a random 50% chance each day of performing diel vertical migration, whereby they descend at dawn to 100 m, and return to the upper layer at dusk. The 75 m active layer is based on the description of vertical distribution in Plourde et al. (2003). Dormant and reproducing late stages are assigned a near-bottom optimal depth (Krumhansl et al. 2018).

A.2. Stage development and molting

Stage development depends on temperature using a Belehradek function (Bělehrádek 1935) with stage-specific coefficients for *C. hyperboreus* (*a_dev*) (Ji et al. 2012), and is reduced under low food conditions based on observations of delayed development of *C. finmarchicus* under low food (Campbell et al. 2001).

$$D = a\_dev \cdot (T + 13.66)^{-2.05} \cdot f\_\mathrm{lim} \tag{A1}$$

f_lim is a Holling Type III response ($F^2/(k_{ff}^2 + F^2)$) applied with a half saturation constant, k_{ff}, of 10.0 μg C L^{-1}, which results in a reduction in development rate of 6%, 10%, 20% and 50% at *in situ* food concentrations of 40, 30, 20, and 10 μg C L^{-1}, respectively.

Molting to the next stage only occurs if the individual structural mass exceeds a stage-specific threshold, based on the values for the "M-Environment" of Bandara et al. (2019) who implemented this strategy to prevent unrealistically small at stage individuals in their model. We use their maximum critical molting masses, *molt_crit* (equivalent to their W_j^{max}), since their evolvable body size parameter always converged to the upper limit.

A.3. Growth, lipid accumulation, starvation

Somatic growth is the balance of carbon inputs and outputs. Input is via ingestion, *I*, modified by the animal's ability to assimilate the ingested food, summarized as the food assimilation coefficient, *a*. Carbon output is via respiration, *R*, and egg production, *EP*. Model formulations for growth and starvation follow Bandara et al. (2019; referred to as B19). The growth rate, *G*, is described in units of μg C ind.$^{-1}$ timestep^{-1} (where the model timestep is 30 min):

$$G = a \cdot I - R - EP \tag{A2}$$

For feeding individuals whose assimilation is greater than their metabolic needs, G>0, and growth occurs. Positive net growth increases structural mass, and for late stages (≥CIII) also contributes to lipid stores. The fraction of net growth that is allocated to lipid stores is 65% (parameter "rate" is fixed at 0.65), although stage CIII which doesn't enter diapause in the GSL is limited to a maximum of 10% dry weight as lipid. Once individuals molt to adult, they can accumulate up to an additional 15% structural mass to represent the changes occurring during the terminal molt, after which structural growth ceases for females while lipid accumulation can continue. Once structural growth ceases in females, 100% of growth is routed to lipid storage. Individuals are able to acquire up to 70% of dry weight as lipid.

Whereas Bandara et al. (2019) calculated lipid mass prognostically in their multi-species model, their simulated *C. hyperboreus* individual lipid

could not evolve freely beyond the cap of 41% of DW as lipid. Those authors specified for stages CIV-CVI an upper limit of up to 70% of structural mass as lipid, which is equivalent to 41% of dry weight as lipid. To simulate observed lipid content for *C. hyperboreus*, late stages can accumulate up to a maximum level of 70% of dry weight as lipid in our model, a cap that was not exceeded by the simulated individuals.

We adopt the treatment of too small stage CIII individuals from Bandara et al. (2019) so as to ensure the smallest individuals grow their structure to a minimum size before initiating lipid storage. Essentially, based on observed ratios of body size to lipid sac volume (Miller et al. 2000, Vogedes et al. 2010), stage CIII individuals smaller than 38 μg C accumulate no lipid, while individuals of at least 159 μg C may accumulate the maximum fraction of growth as lipid (*i.e.*, G×0.65), and for individuals sized in between these limits (38–159 μg C) there is an exponential increase in the fraction of growth routed to lipid, from 0 to 65%. We additionally limit stage CIII individuals to 10% of dry weight as lipid, since this particular stage does not enter diapause in the GSL, and to avoid a potential model problem of small but fatty bodies which (i) is not observed for the species, and (ii) prevents later stages from growing sufficiently large. There are no GSL-based CIII lipid observations to inform CIII lipid content, but CIII individuals preparing to enter diapause in the Arctic have been observed with 25% lipid (Smith 1988) (N=1 in that study) to 42% lipid (Schmid et al. 2018).

Starvation occurs when the instantaneous carbon inputs don't cover the metabolic requirements (*i.e.*, G<0 is starvation, which occurs when I=0 or when I>0 but aI<R; egg production can be ignored in the latter case since I=0 during reproduction)). During starvation, lipid is catabolized to meet the metabolic deficit: if G<0, L(t) = L(t-1) + G×dt. After Bandara et al. (2019), individuals without lipid stores (feeding stages NIII-CII) and late stages whose lipid mass has been depleted are allowed to draw down up to 10% of their structural mass under starvation, although this comes with a penalty of increased mortality risk. Specifically, mortality increases linearly with the percent of structural mass depleted, such that all individuals die once they have drawn down their structural mass by 10%.

A.4. Respiration

Respiration (R, unit = μg C ind.$^{-1}$ timestep^{-1}) is the sum of basal (maintenance, R_b) and activity (swimming, R_a) metabolism, and is applied for non-dormant individuals stage NIII-CVI. For simplicity, egg basal metabolism and non-feeding naupliar (NI-NII) metabolism are neglected. Down regulation of NIII metabolism during periods of starvation was concluded by Jung-Madsen et al. (2013) but there was not enough information in that study to include this in the model. Specific dynamic action, related mainly to protein synthesis, as well as feeding and digestion (Thor 2000), is assumed to be contained in the food assimilation coefficient.

Following Bandara et al. (2019), basal respiration depends on total body size (structural mass + lipid mass) and temperature. At the reference temperature of −2 ℃, basal metabolism scales with the individual's carbon body mass (structural mass *M*+lipid mass *L*):

$$R_{b\_ref} = 0.5 \cdot f \cdot (M + L)^{o} \tag{A3}$$

In the above equation, *f* and *o* are the respiration mass coefficient and exponent, respectively. Respiration increases exponentially with the *in situ* temperature T, as:

$$R_b = R_{b\_ref} \cdot g \cdot \exp(p \cdot T) \tag{A4}$$

with the respiration temperature coefficient and exponent represented in g and p, respectively. Following Bandara et al. (2019), swimming metabolism R_a is 150% of basal metabolism. In the case of dormant individuals, swimming metabolism is zero and basal metabolism is reduced by 75% (=0.25 × R_b). When diapausing females begin egg production, basal metabolism is increased by scaling to the midpoint of active and diapausing (=0.62 × R_b) and swimming metabolism remains at zero, based on visual inspection of reproducing females in the lab that are very sluggish and not moving (S. Plourde, pers. comm.). Note that in our model we reduced the respiration coefficient of mass (parameter *f*) by 10% for all stages, and during diapause stage CIV basal metabolism is further reduced by 25%.

A.5. Ingestion

Ingestion scales with structural mass and ambient food and temperature conditions, using a Type III relationship that reduces ingestion at low and high food concentration, effectively representing food limitation and food satiation (Holling 1965). Ingestion occurs only for active individuals (*i.e.*, not during dormancy or reproduction at depth), and is configured in the model with one-way coupling, as the food forcing is independent of ingestion. Food concentration, *F*, is the sum of large and small phytoplankton and microzooplankton in the GSBM model forcing (Lavoie et al. 2021), which varies spatially (in 1-D only in the vertical) and temporally: here, food fields are instantaneous model output written every 2 days, linearly interpolated to 2-hourly. During the fall months when the *C. hyperboreus* population in the GSL should be entirely in dormancy or reproducing at depth (September – December), we reduced the model food concentration by half.

Following Bandara et al. (2019), at a reference temperature of −2 ℃, ingestion scales with structural mass *M*, where *b* and *m* are the mass ingestion coefficient and exponent:

$$I_{REF} = 0.5 \cdot b \cdot M^{m} \tag{A5}$$

Ingestion increases exponentially with temperature *T*, where *c* and *n* are the temperature coefficient and exponent of ingestion, and in this study is modified by a Holling Type III response ($F^2/(k_f^2 + F^2)$), to the *in situ* food concentration, *F*:

$$I = I_{REF} \cdot c \cdot exp(n \cdot T) \cdot \frac{F^2}{k_f^2 + F^2} \tag{A6}$$

Whereas Bandara et al. (2019) used an asymptotic relationship between food and ingestion with a mass- and food-dependent scaling for food satiation (a modified Holling type II), under such a formulation late stages in our model were still able to grow large despite very low food concentrations, such as before the spring bloom, contrary to observations. Therefore, we implemented a Holling type III term whose sigmoidal curve represents food satiation, and a half-saturation coefficient (k_f) which reduces the ingestion rate to half at the food concentration *F*=27 ug C L^{-1}. The value of k_f was determined from the food concentrations in the GSBM model output, to ensure ingestion remains low during the food scarce period preceding the spring bloom.

A.6. Dormancy

Entry into dormancy in the model depends on the proportion of C dry weight as lipid (*i.e.*, lipid fraction = L/(M+L), where L and M are lipid mass and structural mass, respectively). Active individuals exceeding a threshold lipid fraction enter dormancy at the end of their current stage (*i.e.*, when the molt cycle fraction $\geq$ 0.98), or in the case of adults, after three weeks. The lipid fraction threshold assigned to each particle is sampled from a uniform distribution between 0.33–0.40 for stage CIV (we use increments of 0.01 therefore n = 8), or 0.41–0.47 for stages CV-CVI. The implication of this choice is that CV and CVI individuals must accumulate a higher proportion of lipid in order to trigger the pathway to enter dormancy. The optimization procedure of Bandara et al. (2019) converged for their baseline run (environment "L") on a L/M threshold value of 0.70 for dormancy entry, which is equivalent to 0.41 when transformed into the fraction of dry weight as lipid, L/(M+L), and a proportion of lipid burned of 0.29 for dormancy exit. In their simulations with higher and lower food and temperature and different levels of predation mortality, the optimal dormancy entry parameter value (L/(M+L) = 0.41) remained constant, while the lipid utilization required to exit dormancy varied slightly with environmental changes (0.28–0.31), decreased to 0.22 with intermediate mortality risk, and increased greatly under very high mortality (0.47–0.56).

Observations suggest *C. finmarchicus* CV exit with approximately half of the lipid store remaining, relative to the start of the overwintering period (Ingvarsdóttir et al. 1999). To exit dormancy in the model, the individual must exceed the threshold for lipid utilization. For stages CV-CVI, this threshold is sampled randomly from the uniform distribution 0.44–0.64 (n = 21). For stage CIV which is not preparing to reproduce, a more complete drawdown of lipids occurs in the model in order to reproduce the observed dormancy duration in the GSL of >8 months (July-March), using a higher lipid fraction threshold range: 0.75–0.95. Note that the individual's threshold is located in the same relative position within the uniform range for all stages, such that if assigned 0.44 (0.64) for stages CV-CVI, the individual is therefore assigned 0.75 (0.95) at stage CIV.

A.7. Reproduction: gonad development, maturation, egg production

Reproduction begins in the model once diapausing CV molt to adult at depth, at the end of the CV diapause. In the case of second reproduction females, reproduction begins at the end of diapause, which is described as the drawdown of a specified percentage of the initial lipid reserve at the beginning of diapause. Individual variability in the parameter related to diapause exit signifies that reproduction may begin when females draw down their initial lipid store by a randomly selected value from the 45–65% range.

Female egg production is proportional to the individual's respiration rate, and continues with eggs released in clutches (N=75 eggs) until a lipid lower limit is reached, equal to 15% and 0% of the lipid store at the start of dormancy for first and second reproduction females, respectively. While the matter allocated to eggs is calculated each 30-minute time step, a *daily_eggs* variable is determined daily at midnight. Because assigning the *daily_eggs* to new particles demands large numbers of particles, we therefore assign eggs to a new particle in clutches, once the individual produces 75 eggs, which corresponds to the clutch size mode in Plourde et al. (2003). Spawned eggs that don't achieve a full clutch are not assigned to a new particle, but they are still counted towards the female's cumulative egg production. For example, if a female produces <75 eggs, that female has a non-zero cumulative egg production, but no child particle is created for the offspring to develop and grow. When an egg clutch is released, an "empty" particle is transferred from the edge of the domain to the same position (x, y, z) as the reproducing female. The newly transferred child particle inherits its parameter values from the reproducing female, and its initial abundance is calculated based on 75 eggs/female multiplied by the abundance of females in the mother particle.

A.8. Mortality

In the model, mortality is imposed associated with certain life events (following the molt to adult, males are killed as tracking them decreases computational efficiency, and second reproduction females are spent and die immediately following reproduction). Mortality occurs under starvation in the absence of lipid reserves: mortality increases linearly with catabolization of an individual's structural mass, with 100% mortality at 10% drawdown of structural mass, following Bandara et al. (2019). We did not follow the mortality approach used in Bandara et al. (2019) which emphasized the visual predation mortality term (non-visual predation was set to 10% of visual predation mortality), and positively related visual predation to light and individual size such that large late stages experienced high mortality. Their visual and non-visual predation mortality approach lacked temperature dependence and applied the highest mortality to the largest (most visible or detectable) stages. While causes of *Calanus* spp. mortality and their temporal and spatial variation in the marine environment are highly uncertain, we adopt the observed pattern in *C. finmarchicus* total mortality decreasing with stage and slightly increasing with temperature described as in Ohman et al. (2008). Following the mortality configuration in Maps et al. (2012b), we write an expression for mortality resulting from natural death and predation, *m*, as:

$$m = I^{'} \cdot (0.01 + m1 \cdot \exp(-m2 \cdot stage)) \cdot \left((Tref + 13.66)^{-2.05} \right) / \left((T + 13.66)^{-2.05} \right) \quad \text{(A7)}$$

Here, *m1*, *m2*, and *Tref* are mortality parameters, stage is the integer representing the developmental stage (egg, NI, NII, …CVI correspond to stage 0,1,2, …12), and T is the *in situ* temperature. Mortality scales with temperature based on the ratio of stage duration at a reference temperature to that at the *in situ* temperature, where 13.66 is the species specific offset. The effect of temperature is effectively larger for earlier stages because their first term related to stage is larger (*i.e.*, a 5-fold increase occurs at 12 °C for all stages, but the resulting mortality change is much larger for eggs and early naupliar stages).

While we don't have sufficient knowledge of the GSL predator–prey dynamics to separately model predation, visual detection of prey clearly may be affected by environmental factors like light. Therefore, in the euphotic zone we include a simple mortality adjustment based on the availability of light at the particle depth via a multiplier between 1 (no light) and 1.5 (max light), represented by *I'* in the general mortality equation above. Mortality therefore increases by up to 50% for nauplii and copepodites (not eggs for whom *I'*=1). Light at the particle depth, L(z), is described using GSBM output of surface photosynthetically active radiation (PAR_{surf}) which decays exponentially with depth according to the value of the light attenuation coefficient (k_d):

$$L(z) = PAR_{surf} \cdot \exp(-k_d \cdot z) \quad \text{(A8)}$$

$$\mathrm{I}^{'} = ((\max 2 - \min 2)/(\max 1 - \min 1)) \cdot (\mathrm{L}(z) - \max 1) + \max 2 \quad \text{(A9)}$$

PAR_{surf} varies with solar downwelling shortwave radiation, sea ice and cloud cover and is output at a temporal frequency 12-fold higher than the biological output to resolve diurnal cycles (*i.e.*, for 2-day biological output, PAR_{surf} is 4-hourly, with 12 records produced over 48 h). The expression for *I'* above remaps the light at the particle depth, *L(z)*, to a unitless factor between 1 and 1.5, with *min1* and *max1* representing the range of PAR_{surf} (*min1* = 0 W/m2, *max1* = 360 W/m2), and *min2* and *max2* provide the new factor range limits (*min2* = 1.0, *max2* = 1.5). For simplicity, we use a constant value for $kd = 0.06\ m^{-1}$ which allows visual predation to potentially increase mortality over the upper ~75 m corresponding to the active surface layer. To account for the uncertainty of the simulated vertical positioning within the active layer that we expect to vary with *in situ* food concentration, ambient light, body size, and predation pressure, we implemented the diffuse attenuation coefficient ($kd = 0.06\ m^{-1}$) that under high PAR_{surf} simulates a smooth light decay over the model active layer (0–75 m) instead of representing the observed 20–30 m euphotic zone depth at the Anticosti Gyre in spring and summer (Tian et al. 2000). We assume that copepod nauplii in the GSL are also targeted by visual predators, since they comprised important fractions of the larval fish gut contents of 11 different species on the Newfoundland Shelf (Pepin 2024).

Mortality in the model is the sum of the generic mortality term that encompasses natural death and predation (described above), in addition to starvation mortality that occurs after lipid stores are depleted and structural mass is catabolized, senescence of second reproduction females that are spent following egg production, and the death of males. Following evidence suggesting natural populations are female-dominated (Conover 1965a, Hirche & Niehoff 1996), the model sex ratio is specified as 80% female, 20% male, and the particle abundance is reduced to 80% upon the terminal molt to adult to account for the instantaneous death of males. In the fall months when the entire population in the GSL is observed to be at depth in diapause, we increased the general mortality for late stages still active in the near surface in September-December by applying a factor of 2.25. In the case of late stages either diapausing or reproducing at depth, I' is replaced by 0.1, in line with the observation that mortality for diapausing *C. finmarchicus* was ~10% that of active individuals (McLaren et al. 2001). Mortality coefficients were tuned to produce a quasi-stable model population over 10 years, which requires sufficient survival of the initial population through the first 1–2 years (pre-reproduction), and sufficient loss of the new generation so as to avoid a population explosion. Model mortality therefore varies with stage, activity, temperature, season, and for active stages in the top ~75 m with available light.

Appendix B. Supplementary material

Supplementary data to this article can be found online at https://doi.org/10.1016/j.pocean.2024.103333.

References

Aarflot, J.M., Hjøllo, S.S., Strand, E., Skogen, M.D., 2022. Transportation and predation control structures the distribution of a key calanoid in the Nordic Seas. Prog. Oceanogr. 202 https://doi.org/10.1016/j.pocean.2022.102761.

Aksnes, D.L., Giske, J., 1993. A theoretical model of aquatic visual feeding. Ecol. Model. 67, 233–250. https://doi.org/10.1016/0304-3800(93)90007-F.

Albouy-Boyer, S., Plourde, S., Pepin, P., Johnson, C.L., Lehoux, C., Galbraith, P.S., Hebert, D., Lazin, G., Lafleur, C., 2016. Habitat modelling of key copepod species in the Northwest Atlantic Ocean based on the Atlantic Zone Monitoring Program. J. Plankton Res. fbw020. https://doi.org/10.1093/plankt/fbw020.

Anderson, T.R., Hessen, D.O., Gentleman, W.C., Yool, A., Mayor, D.J., 2022. Quantifying the roles of food intake and stored lipid for growth and development throughout the life cycle of a high-latitude copepod, and consequences for ocean carbon sequestration. Front. Mar. Sci. 9, 1–18. https://doi.org/10.3389/fmars.2022.928209.

Arnkvaern, G., Daase, M., Eiane, K., 2005. Dynamics of coexisting Calanus finmarchicus, Calanus glacialis and Calanus hyperboreus populations in a high-Arctic fjord. Polar Biol. 28, 528–538. https://doi.org/10.1007/s00300-005-0715-8.

Ashjian, C.J., Campbell, R.G., Welch, H.E., Butler, M., Van Keuren, D., 2003. Annual cycle in abundance, distribution, and size in relation to hydrography of important copepod species in the western Arctic Ocean. Deep Res Part I Oceanogr Res Pap 50, 1235–1261. https://doi.org/10.1016/S0967-0637(03)00129-8.

Astthorsson, O.S., Gislason, A., 2003. Seasonal variations in abundance, development and vertical distribution of Calanus finmarchicus, C. hyperboreus and C. glacialis in the East Icelandic Current. J. Plankton Res. 25, 843–854.

Auel, H., Klages, M., Werner, I., 2003. Respiration and lipid content of the Arctic copepod Calanus hyperboreus overwintering 1 m above the seafloor at 2,300 m water depth in the Fram Strait. Mar. Biol. 143, 275–282. https://doi.org/10.1007/s00227-003-1061-4.

Bandara, K., Varpe, Ø., Ji, R., Eiane, K., 2018. A high-resolution modeling study on diel and seasonal vertical migrations of high-latitude copepods. Ecol. Model. 368, 357–376. https://doi.org/10.1016/j.ecolmodel.2017.12.010.

Bandara, K., Varpe, Ø., Ji, R., Eiane, K., 2019. Artificial evolution of behavioral and life history strategies of high-latitude copepods in response to bottom-up and top-down selection pressures. Prog. Oceanogr. 173, 134–164. https://doi.org/10.1016/j.pocean.2019.02.006.

Baumgartner, M.F., Tarrant, A.M., 2017. The physiology and ecology of diapause in marine copepods. Ann. Rev. Mar. Sci. 9, 387–411. https://doi.org/10.1146/annurev-marine-010816-060505.

Bělehrádek, J., 1935. Temperature and living matter. Protoplasma Monogr:1–277.

Benkort, D., Lavoie, D., Plourde, S., Dufresne, C., Maps, F., 2020. Arctic and Nordic krill circuits of production revealed by the interactions between their physiology, swimming behaviour and circulation. Prog. Oceanogr. 182 https://doi.org/10.1016/j.pocean.2020.102270.

Blais, M., Galbraith, P.S., Plourde, S., Devred, E., Clay, S., Lehoux, C., Devine, L., 2021. Chemical and Biological Oceanographic Conditions in the Estuary and Gulf of St. Lawrence during 2020. DFO Can Sci Advis Sec Res Doc.

Brickman, D., Hebert, D., Wang, Z., 2018. Mechanism for the recent ocean warming events on the Scotian Shelf of eastern Canada. Cont. Shelf Res. 156, 11–22. https://doi.org/10.1016/j.csr.2018.01.001.

Budgen, G.L., 1991. Changes in the temperature-salinity characteristics of the deeper waters of the Gulf of St. Lawrence over the past several decades. In: Therriault, J.-C. (Ed.), The Gulf of St. Small Ocean or Big Estuary, Lawrence, pp. 139–147.

Butterfield, R.M., Griffiths, D.A., Thompson, J.M., Zamora, J., James, A.M., 1983. Changes in body composition relative to weight and maturity in large and small strains of Australian Merino rams 1. Muscle, bone and fat. Anim. Sci. 36, 29–37. https://doi.org/10.1017/S0003356100039908.

Campbell, R.G., Wagner, M.M., Teegarden, G.J., Boudreau, C.A., Durbin, E.G., 2001. Growth and development rates in Calanus finmarchicus. Mar. Ecol. Prog. Ser. 221, 161–183. https://doi.org/10.3354/meps221161.

Campbell, R.G., Sherr, E.B., Ashjian, C.J., Plourde, S., Sherr, B.F., Hill, V., Stockwell, D. A., 2009. Mesozooplankton prey preference and grazing impact in the western Arctic Ocean. Deep Res Part II Top Stud Oceanogr 56, 1274–1289. https://doi.org/10.1016/j.dsr2.2008.10.027.

Carlotti, F., Slagstad, D., 1997. Population dynamics model of interacting copepod species coupled with a 1-D model of phytoplankton dynamics in the Greenland Sea Gyre. Environ. Model. Assess. 2, 29–36. https://doi.org/10.1023/a:1019004919035.

Chassé, J., Miller, R.J., 2010. Lobster larval transport in the southern Gulf of St. Lawrence. Fish Oceanogr 19, 319–338. https://doi.org/10.1111/j.1365-2419.2010.00548.x.

Clay, S., Layton, C., Devred, E., 2021. BIO-RSG/PhytoFit: First release (v1.0.0). Zenodo.

Coguiec, E., Last, K., Cohen, J., Hobbs, L., Choquet, M., Ershova, E., Berge, J., Daase, M., 2023. Photoperiodism and overwintering in boreal and sub-Arctic Calanus finmarchicus populations. Mar. Ecol. Prog. Ser. 712, 49–65. https://doi.org/10.3354/meps14307.

Conover, R.J., 1962. Metabolism and growth in Calanus hyperboreus in relation to its life cycle. Rapp Proc-Verb Cons Int Explor Mer 153, 190–197.

Conover, R.J., 1965. Notes On the Molting Cycle, Development of Sexual Characters and Sex Ratio in Calanus Hyperboreus. Crustaceana 8, 308–320. https://doi.org/10.1163/156854065X00497.

Conover, R.J., 1966. Factors affecting the assimilation of organic matter by zooplankton and the question of superfluous feeding. Limnol. Oceanogr. 11, 354–364.

Conover, R.J., 1967. Reproductive cycle, early development, and fecundity in laboratory populations of the copepod Calanus hyperboreus. Crustaceana 13, 61–72. https://doi.org/10.1163/156854067X00080.

Conover, R.J., 1988. Comparative life histories in the genera Calanus and Neocalanus in high latitudes of the northern hemisphere. Hydrobiologia 167 (168), 127–142.

Conover, R.J., Corner, E.D.S., 1968. Respiration and nitrogen excretion by some marine zooplankton in relation to their life cycles. J Mar Biol Assoc United Kingdom 48, 49–75. https://doi.org/10.1017/S0025315400032410.

Conover, R.J., Huntley, M., 1991. Copepods in ice-covered seas - Distribution, adaptations to seasonally limited food, metabolism, growth patterns and life cycle strategies in polar seas. J. Mar. Syst. 2, 1–41. https://doi.org/10.1016/0924-7963(91)90011-l.

Corkett, C.J., McLaren, I.A., 1979. The biology of pseudocalanus. Adv. Mar. Biol. 15, 1–231. https://doi.org/10.1016/S0065-2881(08)60404-6.

Darbyson, E., Swain, D.P., Chabot, D., Castonguay, M., 2003. Diel variation in feeding rate and prey composition of herring and mackerel in the southern Gulf of St Lawrence. J. Fish Biol. 63, 1235–1257. https://doi.org/10.1046/j.1095-8649.2003.00247.x.

Davies, K.T.A., Ryan, A., Taggart, C.T., 2012. Measured and inferred gross energy content in diapausing Calanus spp. in a Scotian shelf basin. J. Plankton Res. 34, 614–625. https://doi.org/10.1093/plankt/fbs031.

Dawson, J.K., 1978. Vertical distribution of Calanus hyperboreus in the central Arctic Ocean. Limnol. Oceanogr. 23, 950–957. https://doi.org/10.4319/lo.1978.23.5.0950.

Dufour, R., Ouellet, P., 2007. Estuary and Gulf of St. Lawrence Marine Ecosystem Overview and Assessment Report. Can Tech Rep Fish Aquat Sci 2744E:vii + 112.

Dupont, N., Aksnes, D.L., 2012. Effects of bottom depth and water clarity on the vertical distribution of Calanus spp. J. Plankton Res. 34, 263–266. https://doi.org/10.1093/plankt/fbr096.

Ejsmond, M.J., McNamara, J.M., Søreide, J., Varpe, Ø., 2018. Gradients of season length and mortality risk cause shifts in body size, reserves and reproductive strategies of determinate growers. Funct. Ecol. 32, 2395–2406. https://doi.org/10.1111/1365-2435.13191.

Falk-Petersen, S., Hopkins, C.C.E., Sargent, J.R., 1990. Trophic relationships in the pelagic, Arctic food web. In: Barnes, M., Gibson, R.N. (Eds.), Trophic Relationship in the Marine Environment. Aberdeen University Press, Aberdeen, Scotland, pp. 315–333.

Falk-Petersen, S., Mayzaud, P., Kattner, G., Sargent, J.R., 2009. Lipids and life strategy of Arctic Calanus. Mar. Biol. Res. 5, 18–39. https://doi.org/10.1080/17451000802512267.

Galbraith, P.S., Chassé, J., Dumas, J., Shaw, J.-L., Caverhill, C., Lefaivre, D., Lafleur, C., 2022. Physical oceanographic conditions in the Gulf of St. Lawrence in 2021.

Gillespie, D.T., 1996. Exact numerical simulation of the Ornstein-Uhlenbeck process and its integral. Phys Rev E - Stat Physics, Plasmas, Fluids, Relat Interdiscip Top 54, 2084–2091. https://doi.org/10.1103/PhysRevE.54.2084.

Gislason, A., 2018. Life cycles and seasonal vertical distributions of copepods in the Iceland Sea. Polar Biol. 41, 2575–2589. https://doi.org/10.1007/s00300-018-2392-4.

Häfker, N.S., Teschke, M., Last, K.S., Pond, D.W., Hüppe, L., Meyer, B., 2018. Calanus finmarchicus seasonal cycle and diapause in relation to gene expression, physiology, and endogenous clocks. Limnol. Oceanogr. 63, 2815–2838. https://doi.org/10.1002/lno.11011.

Harvey, M., Devine, L., 2009. Oceanographic conditions in the Estuary and the Gulf of St. Lawrence during 2008: Zooplankton. DFO Can Sci Advis Sec Res Doc 2009/083:vi + 54 p.

Head, E.J.H., Harris, L.R., 1985. Physiological and biochemical changes in Calanus hyperboreus from Jones Sound NWT during the transition from summer feeding to overwintering condition. Polar Biol. 4, 99–106. https://doi.org/10.1007/BF00442907.

Head, E.J.H., Harris, L.R., Debs, C.A., 1986. Long term grazing experiments with Arctic copepods. J Exp Mar Bio Ecol 100, 271–286. https://doi.org/10.1016/0022-0981(86)90165-6.

Head, E.J.H., Pepin, P., 2010. Spatial and inter-decadal variability in plankton abundance and composition in the Northwest Atlantic (1958–2006). J. Plankton Res. 32, 1633–1648. https://doi.org/10.1093/plankt/fbq090.

Head, E.J.H., Gentleman, W.C., Ringuette, M., 2015. Variability of mortality rates for Calanus finmarchicus early life stages in the Labrador Sea and the significance of egg viability. J. Plankton Res. 37, 1149–1165. https://doi.org/10.1093/plankt/fbv080.

Hirche, H.J., 1991. Distribution of dominant calanoid copepod species in the Greenland sea during late fall. Polar Biol. 11, 351–362. https://doi.org/10.1007/BF00239687.

Hirche, H.-J., 1996. Diapause in the marine copepod, Calanus finmarchicus — a review. Ophelia 44, 129–143. https://doi.org/10.1080/00785326.1995.10429843.

Hirche, J., 1997. Life cycle of the copepod Calanus hyperboreus in the Greenland Sea. Mar. Biol. 128, 607–618.

Hirche, H.J., 1998. Dormancy in three Calanus Species (C. finmarchicus, C. glacialis and C. hyperboreus) from the North Atlantic. Arch Hydrobiol Spec issues Adv Limnol 52, 359–369.

Hirche, H.J., 2013. Long-term experiments on lifespan, reproductive activity and timing of reproduction in the Arctic copepod Calanus hyperboreus. Mar. Biol. 160, 2469–2481. https://doi.org/10.1007/s00227-013-2242-4.

Hirche, H.J., Niehoff, B., 1996. Reproduction of the Arctic copepod Calanus hyperboreus in the Greenland Sea-field and laboratory observations. Polar Biol. 16, 209–219. https://doi.org/10.1007/s003000050046.

Hirst, A.G., Kiørboe, T., 2002. Mortality of marine planktonic copepods: Global rates and patterns. Mar. Ecol. Prog. Ser. 230, 195–209. https://doi.org/10.3354/meps230195.

Holling, C.S., 1965. The functional response of predators to prey density and its role in mimicry and population regulation. Mem Entomol Soc Can 45, 5–60. https://doi.org/10.4039/entm9745fv.

Huntley, M.E., Lopez, M.D.G., 1992. Temperature-Dependent Production of Marine Copepods : A Global Synthesis. Am. Nat. 140, 201–242.

Ikeda, T., Kanno, Y., Ozaki, K., Shinada, A., 2001. Metabolic rates of epipelagic marine copepods as a function of body mass and temperature. Mar. Biol. 139, 587–596. https://doi.org/10.1007/s002270100608.

Ingvarsdóttir, A., Houlihan, D.F., Heath, M.R., Hay, S.J., 1999. Seasonal changes in respiration rates of copepodite stage V Calanus finmarchicus (Gunnerus). Fish. Oceanogr. 8, 73–83. https://doi.org/10.1046/j.1365-2419.1999.00002.x.

Ji, R., Ashjian, C.J., Campbell, R.G., Chen, C., Gao, G., Davis, C.S., Cowles, G.W., Beardsley, R.C., 2012. Life history and biogeography of Calanus copepods in the Arctic Ocean: An individual-based modeling study. Prog. Oceanogr. 96, 40–56. https://doi.org/10.1016/j.pocean.2011.10.001.

Johnson, C.L., Leising, A.W., Runge, J.A., Head, E.H.J., Pepin, P., Plourde, S., Durbin, E. G., 2008. Characteristics of Calanus finmarchicus dormancy patterns in the Northwest Atlantic. ICES J. Mar. Sci. 65, 339–350. https://doi.org/10.1093/icesjms/fsm171.

Jónasdóttir, S.H., 1999. Lipid content of Calanus finmarchicus during overwintering in the Faroe-Shetland Channel. Fish. Oceanogr. 8, 61–72. https://doi.org/10.1046/j.1365-2419.1999.00003.x.

Jung-Madsen, S., Nielsen, T.G., Grønkjær, P., Hansen, B.W., Møller, E.F., 2013. Early development of Calanus hyperboreus nauplii: Response to a changing ocean. Limnol. Oceanogr. 58, 2109–2121. https://doi.org/10.4319/lo.2013.58.6.2109.

Kiørboe, T., 2008. Zooplankton feeding rates and bioenergetics. In: *A Mechanistic Approach to Plankton Ecology*. Princeton University Press, p 101–121.

Kosobokova, K.N., 1999. The reproductive cycle and life history of the Arctic copepod Calanus glacialis in the White Sea. Polar Biol. 22, 254–263. https://doi.org/10.1007/s003000050418.

Kosobokova, K.N., Hanssen, H., Hirche, H.J., Knickmeier, K., 1997. Composition and distribution of zooplankton in the Laptev Sea and adjacent Nansen Basin during summer, 1993. Polar Biol. 19, 63–76. https://doi.org/10.1007/s003000050216.

Koutitonsky, V.G., Bugden, G.L., 1991. The physical oceanography of the Gulf of St. Lawrence: A review with emphasis on the synoptic variability of the motion, In J.-C. Therriault [ed.] The Gulf of St. Lawrence: small ocean or big estuary? Can. Spec. Publ. Fish. Aquat. Sci. 113, 57–90.

Krumhansl, K.A., Head, E.J.H., Pepin, P., Plourde, S., Record, R., Runge, J.A., Johnson, C. L., 2018. Environmental drivers of vertical distribution in diapausing Calanus copepods in the northwest Atlantic. Prog. Oceanogr. 162, 202–222. https://doi.org/10.1016/j.pocean.2018.02.018.

Kvile, K.Ø., Ashjian, C., Feng, Z., Zhang, J., Ji, R., 2018. Pushing the limit: Resilience of an Arctic copepod to environmental fluctuations. Glob. Chang. Biol. 24, 5426–5439. https://doi.org/10.1111/gcb.14419.

Laliberté, J., Larouche, P., 2023. Chlorophyll-a concentration climatology, phenology, and trends in the optically complex waters of the St. Lawrence Estuary and Gulf. J Mar Syst 238. https://doi.org/10.1016/j.jmarsys.2022.103830.

Lavoie, D., Chassé, J., Simard, Y., Lambert, N., Galbraith, P.S., Roy, N., Brickman, D., 2016. Large-Scale Atmospheric and Oceanic Control on Krill Transport into the St. Lawrence Estuary Evidenced with Three-Dimensional Numerical Modelling. Atmos. Ocean 54, 299–325. https://doi.org/10.1080/07055900.2015.1082965.

Lavoie, D., Lambert, N., Rousseau, S., Dumas, J., Chassé, J., Long, Z., Perrie, W., Starr, M., Brickman, D., Azetsu-Scott, K., 2020. Projections of future physical and biogeochemical conditions in the Gulf of St. Lawrence, on the Scotian Shelf and in the Gulf of Maine using a regional climate model. Can Tech Rep Hydrogr Ocean Sci 334:xiii + 102 p.

Lavoie, D., Lambert, N., Starr, M., Chassé, J., Riche, O., Le Clainche, Y., Azetsu-Scott, K., Béjaoui, B., Christian, J.R., Gilbert, D., 2021. The Gulf of St. Lawrence Biogeochemical Model: A Modelling Tool for Fisheries and Ocean Management. Front. Mar. Sci. 8, 1–29. https://doi.org/10.3389/fmars.2021.732269.

Le Corre, N., Brennan, C.E., Chassé, J., Johnson, C.L., Lavoie, D., Paquin, J.-P., Soontiens, N., Plourde, S., 2023. A biophysical model of Calanus hyperboreus in the Gulf of St. Lawrence: Interannual variability in phenology and circulation drive the timing and location of right whale foraging habitat in spring and early summer. Prog. Oceanogr. 219, 1–20. https://doi.org/10.1016/j.pocean.2023.103152.

Lee, R.F., 1974. Lipid composition of the copepod Calanus hyperboreas from the Arctic Ocean. Changes with depth and season. Mar. Biol. 26, 313–318. https://doi.org/10.1007/BF00391515.

Lee, R.F., Hagen, W., Kattner, G., 2006. Lipid storage in marine zooplankton. Mar. Ecol. Prog. Ser. 307, 273–306. https://doi.org/10.3354/meps307273.

Lehoux, C., Plourde, S., Lesage, V., 2020. Significance of dominant zooplankton species to the North Atlantic Right Whale potential foraging habitats in the Gulf of St. Lawrence: a bio-energetic approach. DFO Can Sci Advis Sec Res. Doc.:iv + 44 p.

Longhurst, A., Sameoto, D., Herman, A., 1984. Vertical distribution of arctic zooplankton in summer: Eastern Canadian archipelago. J. Plankton Res. 6, 137–168. https://doi.org/10.1093/plankt/6.1.137.

Maps, F., Plourde, S., Zakardjian, B., 2010. Control of dormancy by lipid metabolism in Calanus finmarchicus: A population model test. Mar. Ecol. Prog. Ser. 403, 165–180. https://doi.org/10.3354/meps08525.

Maps, F., Runge, J.A., Leising, A., Pershing, A.J., Record, N.R., Plourde, S., Pierson, J.J., 2012a. Modelling the timing and duration of dormancy in populations of Calanus finmarchicus from the Northwest Atlantic shelf. J. Plankton Res. 34, 36–54. https://doi.org/10.1093/plankt/fbr088.

Maps, F., Pershing, A.J., Record, N.R., 2012b. A generalized approach for simulating growth and development in diverse marine copepod species. ICES J. Mar. Sci. 69, 370–379. https://doi.org/10.1093/icesjms/fsr182 A.

Maps, F., Record, N.R., Pershing, A.J., 2014a. A metabolic approach to dormancy in pelagic copepods helps explaining inter- and intra-specific variability in life-history strategies. J. Plankton Res. 36, 18–30. https://doi.org/10.1093/plankt/fbt100.

Maps, F., Plourde, S., Lavoie, D., McQuinn, I., Chassé, J., 2014b. Modelling the influence of daytime distribution on the transport of two sympatric krill species (Thysanoessa raschii and Meganyctiphanes norvegica) in the Gulf of St Lawrence, eastern Canada. ICES J. Mar. Sci. 71, 282–292. https://doi.org/10.1093/icesjms/fst021.

McLaren, I.A., Head, E., Sameoto, D.D., 2001. Life cycles and seasonal distributions of Calanus finmarchicus on the central Scotian Shelf. Can. J. Fish. Aquat. Sci. 58, 659–670. https://doi.org/10.1139/cjfas-58-4-659.

Mei, Z.-P., Lavoie, D., Lambert, N., Starr, M., Chassé, J., Perrie, W., Long, Z., 2024. Modelling the bottom-up effects of climate change on primary production in the Gulf of St. Lawrence and eastern Scotian Shelf. Front Mar Sci 11:1416744. https://doi.org/10.3389/fmars.2024.1416744.

Melle, W., Skjoldal, H.R., 1998. Reproduction and development of Calanus finmarchicus, C. glacialis and C. hyperboreus in the Barents Sea. Mar. Ecol. Prog. Ser. 169, 211–228. https://doi.org/10.3354/meps169211.
Miller, C.B., Cowles, T.J., Wiebe, P.H., Copley, N.J., Grigg, H., 1991. Phenology in Calanus finmarchicus; hypotheses about control mechanisms. Mar. Ecol. Prog. Ser. 72, 79–91. https://doi.org/10.3354/meps072079.
Miller, C.B., Lynch, D.R., Carlotti, F., Gentleman, W., Lewis, C.V.W., 1998. Coupling of an individual-based population dynamic model of Calanus finmarchicus to a circulation model for the Georges Bank region. Fish. Oceanogr. 7, 219–234. https://doi.org/10.1046/j.1365-2419.1998.00072.x.
Miller, C.B., Crain, J.A., Morgan, C.A., 2000. Oil storage variability in Calanus finmarchicus. ICES J. Mar. Sci. 57, 1786–1799. https://doi.org/10.1006/jmsc.2000.0975.
Niehoff, B., Hirche, H.J., 2005. Reproduction of Calanus glacialis in the Lurefjord (western Norway): indication for temperature-induced female dormancy. Mar. Ecol. Prog. Ser. 285, 107–115. https://doi.org/10.3354/meps285107.
Ohashi, K., Sheng, J., 2013. Influence of St. Lawrence River discharge on the circulation and hydrography in Canadian Atlantic waters. Cont. Shelf Res. 58, 32–49. https://doi.org/10.1016/j.csr.2013.03.005.
Ohman, M.D., Runge, J.A., Durbin, E.G., Field, D.B., Niehoff, B., 2002. On birth and death in the sea. Hydrobiologia 480, 55–68. https://doi.org/10.1023/A:1021228900786.
Ohman, M.D., Eiane, K., Durbin, E.G., Runge, J.A., Hirche, H.J., 2004. A comparative study of Calanus finmarchicus mortality patterns at five localities in the North Atlantic. ICES J. Mar. Sci. 61, 687–697. https://doi.org/10.1016/j.icesjms.2004.03.016.
Ohman, M.D., Romagnan, J.B., 2016. Nonlinear effects of body size and optical attenuation on Diel Vertical Migration by zooplankton. Limnol. Oceanogr. 61, 765–770. https://doi.org/10.1002/lno.10251.
Pasternak, A., Arashkevich, E., Tande, K., Falkenhaug, T., 2001. Seasonal changes in feeding, gonad development and lipid stores in Calanus finmarchicus and C. hyperboreus from Malangen, northern Norway. Mar. Biol. 138, 1141–1152. https://doi.org/10.1007/s002270100553.
Pawlowicz, R., 2020. "M_Map: A mapping package for MATLAB", version 1.4m, [Computer software], available online at https://www.eoas.ubc.ca/~rich/map.html.
Pepin, P., 2024. Foraging by larval fish: a full stomach is indicative of high performance but random encounters with prey are also important. ICES J. Mar. Sci. 1–17. https://doi.org/10.1093/icesjms/fsae037.
Pierson, J.J., Batchelder, H., Saumweber, W., Leising, A., Runge, J., 2013. The impact of increasing temperatures on dormancy duration in Calanus finmarchicus. J. Plankton Res. 35, 504–512. https://doi.org/10.1093/plankt/fbt022.
Plourde, S., Starr, M., Devine, L., St-Pierre, J.-F., St-Amand, L., Joly, P., Galbraith, P.S., 2014. Chemical and biological oceanographic conditions in the Estuary and Gulf of St. Lawrence during 2011 and 2012. DFO Can Sci Advis Sec Res Doc 2014/049:v + 46 p.
Plourde, S., Joly, P., Runge, J.A., Dodson, J., Zakardjian, B., 2003. Life cycle of Calanus hyperboreus in the lower St. Lawrence Estuary and its relationship to local environmental conditions. Mar. Ecol. Prog. Ser. 255, 219–233.
Plourde, S., Lehoux, C., Johnson, C.L., Perrin, G., Lesage, V., 2019. North Atlantic right whale (Eubalaena glacialis) and its food: (I) a spatial climatology of Calanus biomass and potential foraging habitats in Canadian waters. J. Plankton Res. 41, 667–685. https://doi.org/10.1093/plankt/fbz024.
Record, N.R., Pershing, A.J., Runge, J.A., Mayo, C.A., Monger, B.C., Chen, C., 2010. Improving ecological forecasts of copepod community dynamics using genetic algorithms. J. Mar. Syst. 82, 96–110. https://doi.org/10.1016/j.jmarsys.2010.04.001.
Rey-Rassat, C., Irigoien, X., Harris, R., Carlotti, F., 2002. Energetic cost of gonad development in Calanus finmarchicus and C. helgolandicus. Mar. Ecol. Prog. Ser. 238, 301–306. https://doi.org/10.3354/meps238301.
Ringuette, M., Fortier, L., Fortier, M., Runge, J.A., Bélanger, S., Larouche, P., Weslawski, J.M., Kwasniewski, S., 2002. Advanced recruitment and accelerated population development in Arctic calanoid copepods of the North Water. Deep Res Part II Top Stud Oceanogr 49, 5081–5099. https://doi.org/10.1016/S0967-0645(02)00179-0.
Runge, J.A., Castonguay, M., De Lafontaine, Y., Ringuette, M., Beaulieu, J.L., 1999. Covariation in climate, zooplankton biomass and mackerel recruitment in the southern Gulf of St Lawrence. Fish. Oceanogr. 8, 139–149. https://doi.org/10.1046/j.1365-2419.1999.00095.x.
Saha, S., Moorthi, S., Pan, H.L., Wu, X., Wang, J., Nadiga, S., Tripp, P., Kistler, R., Woollen, J., Behringer, D., Liu, H., Stokes, D., Grumbine, R., Gayno, G., Wang, J., Hou, Y.T., Chuang, H.Y., Juang, H.M.H., Sela, J., Iredell, M., Treadon, R., Kleist, D., Van Delst, P., Keyser, D., Derber, J., Ek, M., Meng, J., Wei, H., Yang, R., Lord, S., Van Den Dool, H., Kumar, A., Wang, W., Long, C., Chelliah, M., Xue, Y., Huang, B., Schemm, J.K., Ebisuzaki, W., Lin, R., Xie, P., Chen, M., Zhou, S., Higgins, W., Zou, C. Z., Liu, Q., Chen, Y., Han, Y., Cucurull, L., Reynolds, R.W., Rutledge, G., Goldberg, M., 2010. The NCEP climate forecast system reanalysis. Bull. Am. Meteorol. Soc. 91, 1015–1057. https://doi.org/10.1175/2010BAMS3001.1.
Saha, S., Moorthi, S., Wu, X., Wang, J., Nadiga, S., Tripp, P., Behringer, D., Hou, Y.T., Chuang, H.Y., Iredell, M., Ek, M., Meng, J., Yang, R., Mendez, M.P., Van Den Dool, H., Zhang, Q., Wang, W., Chen, M., Becker, E., 2014. The NCEP climate forecast system version 2. J. Clim. 27, 2185–2208. https://doi.org/10.1175/JCLI-D-12-00823.1.
Sameoto, D., Herman, A., 1990. Life cycle and distribution of Calanus finmarchicus in deep basins on the Nova Scotia shelf and seasonal changes in Calanus spp. Mar. Ecol. Prog. Ser. 66, 225–237.
Saumweber, W.J., Durbin, E.G., 2006. Estimating potential diapause duration in Calanus finmarchicus. Deep Res Part II Top Stud Oceanogr 53, 2597–2617. https://doi.org/10.1016/j.dsr2.2006.08.003.
Savenkoff, C., Castonguay, M., Chabot, D., Hammill, M.O., Bourdages, H., Morissette, L., 2007. Changes in the northern Gulf of St. Lawrence ecosystem estimated by inverse modelling: Evidence of a fishery-induced regime shift? Estuar. Coast. Shelf Sci. 73, 711–724. https://doi.org/10.1016/j.ecss.2007.03.011.
Schmid, M.S., Maps, F., Fortier, L., 2018. Lipid load triggers migration to diapause in Arctic Calanus copepods — insights from underwater imaging. J. Plankton Res. 40, 311–325. https://doi.org/10.1093/plankt/fby012.
Schultz, M., Nielsen, T.G., Møller, E.F., 2020. The importance of temperature and lipid accumulation for initiation and duration of Calanus hyperboreus spawning. J. Plankton Res. 42, 159–171. https://doi.org/10.1093/plankt/fbaa003.
Scott, C.L., Kwasniewski, S., Falk-Petersen, S., Sargent, J.R., 2000. Lipids and life strategies of Calanus finmarchicus, Calanus glacialis and Calanus hyperboreus in late autumn, Kongsfjorden, Svalbard. Polar Biol. 23, 510–516. https://doi.org/10.1007/s003000000114.
Skottene, E., Tarrant, A.M., Altin, D., Olsen, R.E., Choquet, M., Kvile, K., 2020. Lipid metabolism in Calanus finmarchicus is sensitive to variations in predation risk and food availability. Sci. Rep. 10, 1–14. https://doi.org/10.1038/s41598-020-79165-6.
Smith, S.L., 1988. Copepods in Fram Strait in summer: distribution, feeding and metabolism. J. Mar. Res. 46, 145–181. https://doi.org/10.1357/002224088785113720.
Smith, S.L., 1990. Egg production and feeding by copepods prior to the spring bloom of phytoplankton in Fram Strait, Greenland Sea. Mar. Biol. 106, 59–69. https://doi.org/10.1007/BF02114675.
Sømme, J.D., 1934. Animal plankton of the Norwegian coast waters and the open sea. I. Production of Calanus finmarchicus (Gunner) and Calanus hyperboreus (Krøyer) in the Lofoten Area. Fisk Skr Havundersok (Report Nor Fish Mar Investig 4:1–163.
Sorochan, K.A., Plourde, S., Morse, R., Pepin, P., Runge, J., Thompson, C., Johnson, C.L., 2019. North Atlantic right whale (Eubalaena glacialis) and its food: (II) interannual variations in biomass of Calanus spp. on western North Atlantic shelves. J. Plankton Res. 41, 687–708. https://doi.org/10.1093/plankt/fbz044.
Sorochan, K.A., Plourde, S., Johnson, C.L., 2023. Near-bottom aggregations of Calanus spp. copepods in the southern Gulf of St. Lawrence in summer: significance for North Atlantic right whale foraging. ICES J Mar Sci:1–16. https://doi.org/10.1093/icesjms/fsad003.
Stearns, A.S.C., 1989. Trade-offs in life-history evolution. Funct. Ecol. 3, 259–268.
Takahashi, K., Nagao, N., Taguchi, S., 2002. Respiration of adult female Calanus hyperboreus (Copepoda) during spring in the North Water Polynya. Polar Biosci 15, 45–51.
Takahashi, K., Ichinomiya, M., Okazaki, Y., Nishibe, Y., 2023. Higher ingestion rates and importance of ciliates in the diet of a large, subarctic copepod revealed by larger volume incubations. Limnol Oceanogr:790–802. https://doi.org/10.1002/lno.12310.
Tande, K.S., Slagstad, D., 1985. Assimilation efficiency in herbivorous aquatic organisms—The potential of the ratio method using 14C and biogenic silica as markers. Limnol. Oceanogr. 30, 1093–1099. https://doi.org/10.4319/lo.1985.30.5.1093.
Therriault, J.-C., Petrie, B., Pepin, P., Gagnon, J., Gregory, D., Helbig, J., Herman, A., Lefaivre, D., Mitchell, M., Pelchat, B., Runge, J., Sameoto, D., 1998. Proposal for a northwest zonal monitoring program. Can Tech Rep Hydrogr. Ocean Sci. 194, vii + 57 p.
Thor, P., 2000. Relationship between specific dynamic action and protein deposition in calanoid copepods. J Exp Mar Bio Ecol 245, 171–182. https://doi.org/10.1016/S0022-0981(99)00159-8.
Tian, R.C., Vézina, A., Legendre, L., Ingram, R.G., Klein, B., Packard, T., Roy, S., Savenkoff, C., Silverberg, N., Therriault, J.C., Tremblay, J.E., 2000. Effects of pelagic food-web interactions and nutrient remineralization on the biogeochemical cycling of carbon: A modeling approach. Deep Res Part II Top Stud Oceanogr 47, 637–662. https://doi.org/10.1016/S0967-0645(99)00121-6.
Tokuhiro, K., Matsuno, K., Onodera, J., Sampei, M., Fujiwara, A., Harada, N., Niehoff, B., Nöthig, E., Yamaguchi, A., 2024. Sediment trap samples reveal regional differences in the population structure of Calanus hyperboreus from the Arctic Ocean. J. Plankton Res. 00, 1–11. https://doi.org/10.1093/plankt/fbad059.
Trites, R.W., Walton, A., 1975. A Canadian Coastal Sea - The Gulf of St. Lawrence, Dartmouth, Nova Scotia.
Uhlenbeck, G.E., Ornstein, L.S., 1930. On the theory of the Brownian motion. Phys. Rev. 36, 823–841. https://doi.org/10.1103/PhysRev.36.823.
Varpe, Ø., 2017. Life history adaptations to seasonality. Integr. Comp. Biol. 57, 943–960. https://doi.org/10.1093/icb/icx123.
Varpe, Ø., Ejsmond, M.J., 2018a. In: Semelparity and iteroparity. Oxford Univerity Press, pp. 97–124.
Varpe, Ø., Ejsmond, M.J., 2018b. Trade - offs between storage and survival affect diapause timing in capital breeders. Evol. Ecol. 32, 623–641. https://doi.org/10.1007/s10682-018-9961-4.
Vesin, J.-P., Leggett, W.C., Able, K.W., 1981. Feeding Ecology of Capelin (Mallotus villosus) in the Estuary and Western Gulf of St. Lawrence and its Multispecies implications. Can. J. Fish. Aquat. Sci. 38, 257–267.
Visser, A.W., Grønning, J., Jónasdóttir, S.H., 2017. Calanus hyperboreus and the lipid pump. Limnol. Oceanogr. 62, 1155–1165. https://doi.org/10.1002/lno.10492.
Vogedes, D., Varpe, Ø., Søreide, J.E., Graeve, M., Berge, J., Falk-Petersen, S., 2010. Lipid sac area as a proxy for individual lipid content of arctic calanoid copepods. J. Plankton Res. 32, 1471–1477. https://doi.org/10.1093/plankt/fbq068.